Static morphogen scaling enables proportional growth in tissue growth model inspired by axolotl limb regeneration

Natalia Lyubaykina[a], Dunja Knapp[b,c,1], Pietro Tardivo[d], Maximilian Kotz[a], Tatiana Sandoval-Guzmán[b,e,c,1], and Benjamin M. Friedrich[a,1]

[a]Cluster of Excellence 'Physics of Life', TU Dresden, Dresden, Germany

[b]Department of Internal Medicine III, University Hospital Carl Gustav Carus, TU Dresden, Dresden, Germany
[c]Paul Langerhans Institute Dresden, Helmholtz Centre Munich at TU Dresden, Dresden, Germany

[d]Institute of Molecular Biotechnology of the Austrian Academy of Sciences (IMBA), Vienna BioCenter (VBC), Vienna, Austria
[e]Center for Regenerative Therapies Dresden, TU Dresden, Dresden, Germany

Axolotls can regenerate lost limbs throughout their lives, while they continue to grow. This poses the question of how the size and pattern of a regenerating limb is matched to a widely varying animal size. Two interacting signaling molecules, SHH and FGF8, are produced at opposite sides of the regenerating limb and sustain tissue growth through a pair of oppositely-oriented signaling gradients. As the size of the regrowing tissue can vary more than three-fold depending on the size of the animal, it is unclear how the activities of these mutually dependent morphogens are maintained and subsequently terminated to determine appropriate growth. Scaling of limb regeneration suggests a size-dependent adaptation of morphogen gradient parameters. Inspired by this biological example, we theoretically investigate general mechanisms of morphogen-controlled growth arrest and proportional growth. In the proposed mechanism, tissue growth increases the spatial distance between the two morphogen gradients, thus providing negative feedback that eventually arrests morphogen activity and growth. We put forward two distinct scaling scenarios of morphogen gradients: either dynamic scaling with blastema size, where morphogen gradient parameters change dynamically with the growing tissue, or static scaling with animal size, where morphogen gradient parameters stay constant during blastema growth and only depend on animal size. We show that static scaling ensures proportional growth, but dynamic scaling does not. We compare theory predictions to experimental quantification of SHH and FGF8 morphogen gradient parameters at different time-points of regeneration in different-sized animals, indicating static scaling for some morphogen parameters, which is sufficient to ensure proportional growth in our model.

regeneration | axolotl | adaptive morphogenesis | growth control | morphogen gradient scaling

Correspondence: *benjamin.m.friedrich@tu-dresden.de, tatiana.sandoval_guzman@tu-dresden.de, dunja.knapp@tu-dresden.de*

Introduction

Axolotls possess remarkable regenerative capabilities, including the ability to regenerate fully functional limbs even in adulthood (1). Limb regeneration shares similarities with limb development (2; 3), which is largely conserved among vertebrates (4). However, limb regeneration must also cope with the different sizes of juvenile and adult animals, which can differ up to ten-fold in linear size (5). Regeneration to match animal size represents a general open problem of adaptive morphogenesis (6). Limb regeneration in axolotls starts with wound closure after limb loss, followed by the formation of a bud called blastema consisting of undifferentiated progenitor cells, growth of this blastema, and eventually cell differentiation to give rise to various limb tissues (Fig. 1B). Blastema growth depends on animal size (Fig. 1C; wide-field images of corresponding stages, see Fig. S1). The result of the first phase of blastema growth is a hypometric limb (called "tiny limb" in (7)). This hypometric limb subsequently grows to its final size in a second growth phase, which is particularly pronounced in larger animals (7).

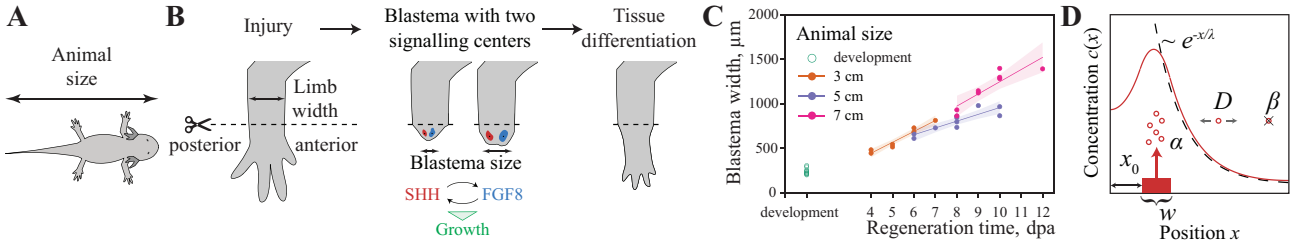

Figure 1. *Axolotl limb regeneration. A.* Schematic of an axolotl, with definition of snout-to-tail animal size. *B.* Schematic of axolotl limb regeneration, highlighting its key stages: After limb amputation, a blastema with two distinct signaling centers producing SHH posteriorly (red) and FGF8 anteriorly (blue) forms. These mutually reinforcing morphogens induce cell proliferation, and thus regulate blastema growth. After this first growth phase of blastema growth, tissue differentiation and additional growth completes limb regeneration. Dashed line indicates amputation plane, arrows indicate limb and blastema size. *C.* Blastema size at subsequent time points (days post amputation, dpa) for animals of different size (filled symbols), and development (open symbols; measured along a line passing through the centers of SHH and FGF source regions in 3D images, see Methods for details). *D.* Morphogen gradient described by minimal reaction-diffusion model Eq. (1) together with visualization of model parameters.

We will focus on the first growth phase of limb regeneration, *blastema growth*. The sizes of same-stage blastemas scale with animal size (8). This scaling is not perfectly proportional, but allometric, i.e., blastema size does not increase linearly with animal size, but according to a power-law with exponent 0.6 (8) (see also Fig. S2 in SI appendix). In contrast, intact limb size is proportional to animal size across a wide range of animal sizes (8) (see also Fig. S3 in SI appendix). Thus, the relative size of the blastema is smaller in larger animals. For the smaller animals considered here, proportional scaling is an appropriate approximation.

Blastema growth involves a pair of oppositely-oriented morphogen gradients. Like the developing limb bud, the regenerating blastema display two signaling centers that secrete morphogens: a posterior center expressing SHH (Sonic Hedgehog) (9; 10), and an anterior center expressing FGF8 (Fibroblast Growth Factor) (11; 12), which mutually reinforce each other's expression (13; 14; 15). In intact mature limbs, SHH and FGF8 are undetectable (16; 17) (see also Fig. S4 in SI appendix). However, following injury, their production is activated, with clear evidence that both SHH and FGF8 are essential for maintaining blastema growth and successful limb regeneration (17; 11; 9). Because of their mutual feedback, the individual roles of SHH and FGF8 in regulating cell proliferation are challenging to disentangle. While neither morphogen alone seems sufficient to support growth and regeneration in ectopically induced blastemas *in vivo* (17), both enhance proliferation individually and additively in cultured dissociated blastema cells *in vitro* (8). Consequently, it remains challenging to determine whether one or both morphogens directly up-regulate proliferation.

Here, we focus on the stage of blastema growth as a paradigmatic model system for morphogen-dependent growth control and growth arrest in animals of different sizes. Recently, the sizes of the source regions of SHH and FGF8 were measured by chromogenic RNA *in situ* stainings in thin sections of middle-stage blastemas of animals of different sizes, indicating allometric scaling of source regions with animal size at the chosen time-point (8). Inspired by this, we explore a minimal mathematical model of coupled tissue growth and morphogen dynamics in a system of two morphogens to identify physical mechanisms that ensure robust growth arrest and proportional growth. We systematically dissect differences between two fundamental growth rules based on either one or two morphogens, as well as two scaling scenarios of morphogen gradients, scaling either *dynamically* with growing blastema size, or *statically* with animal size. Our theoretical analysis singles out a mechanism of growth control by two oppositely-oriented morphogen gradients, where at least some morphogen gradient parameters must exhibit static scaling to enable proportional growth. By combining whole mount *in situ* hybridization with tissue clearing and confocal microscopy (18), we quantify the three-dimensional size of SHH and FGF8 morphogen sources as function of time in regenerating blastemas of different-sized animals, as well as the FGF8 signaling range by measuring the expression of its down-stream target *Dusp6*. We found that some gradient parameters (FGF8 source size) scale *statically* with animal size, while others scale *dynamically* with blastema size. Such scaling is sufficient to ensure proportional growth in our model.

Results

Coupling morphogen dynamics and growth

As a minimal model of morphogen dynamics in a growing blastema, we consider a one-dimensional system of size L, see Fig. 1D. We first introduce notation for the simple case of a single morphogen. The morphogen is produced

within a source region of width w (located at a distance x_0 from the tissue boundary), subsequently diffuses through the tissue with effective diffusion coefficient D, while undergoing degradation with degradation rate β. The dynamics of morphogen concentration $c(x,t)$ as function of time t is then given by

$$\partial_t c(x,t) = D\,\partial_x^2 c(x,t) - \beta c(x,t) + \alpha\,\chi_w(x) \quad . \tag{1}$$

Here, the source function $\chi_w(x)$ characterizes the shape of the morphogen source, which we assume to take the value 1 inside the interval $[x_0, x_0+w]$ and zero outside. The rate total of morphogen production is thus $j = \alpha w$, with units of molecules per time. The steady-state morphogen concentration profile $c^*(x)$ that is established at long times is thus fully defined by five parameters, which set its amplitude A and a characteristic pattern length-scale λ. This pattern length-scale is determined by a competition between the diffusion coefficient D and the degradation rate β

$$\lambda = \sqrt{\frac{D}{\beta}} \quad . \tag{2}$$

The steady-state concentration gradient $c^*(x)$ approximately follows an exponentially decaying profile with this pattern length-scale λ

$$c^*(x) \approx \frac{\alpha w}{\sqrt{D\beta}} \exp\left(-\frac{x}{\lambda}\right) \quad . \tag{3}$$

This approximation becomes exact when the morphogen source is small, localized on the system's boundary, and the system is large. Analytic formulas for more realistic cases are given in SI appendix, Eq. (S18). Generally, concentrations are higher in smaller, bounded systems, as morphogens spread in a smaller domain. This size-dependence of morphogen concentrations will become important in our model, once morphogens control growth.

Eq. (1) generalizes in a straightforward manner to the case of two morphogens with respective concentration fields $s(x,t)$ and $f(x,t)$ instead of $c(x,t)$ in Eq. (1), where $s(x)$ and $f(x)$ can be thought of as the concentrations of SHH and FGF8 morphogens. For conceptual clarity, we consider a symmetric case of two morphogens with identical kinetic parameters and mirror-symmetric source regions (see SI appendix, Eqs. (S24-25) for their formulas analogous to Eq. (1)). The general case of not-identical parameters for two morphogens is qualitatively similar.

To address the dynamics in growing tissue, we consider a one-dimensional tissue that grows with local growth rate $g(x,t)$. Tissue growth convects the concentration field $c(x,t)$ of morphogen with velocity $v(x,t)$ where $\partial_x v = g$, as well as dilutes local morphogen concentration at rate g (see Methods).

Growth control by one or two morphogens

Two interacting morphogens, SHH and FGF8, are implicated in regulating cell proliferation in axolotl limb development and regeneration (8; 17). Due to the mutual feedback between these two morphogens, inactivating one consequently inactivates the other. Therefore, it is experimentally difficult to determine if the direct signal from just one or from both morphogens is needed to promote proliferation. To theoretically explore both cases, we define two putative growth rules, both of which are inspired by a switch-like control of cell behavior as function of local morphogen concentration (19). Specifically, we assume that the tissue grows locally if morphogen concentrations are above a threshold:

One-morphogen growth rule: the tissue grows at the position x if (and only if) the concentration $c(x)$ of a morphogen is above a fixed threshold Θ, see Fig. 2A.

Two-morphogen growth rule: the tissue grows at the position x if the concentrations of both morphogens, $s(x)$ and $f(x)$ (e.g., SHH and FGF8) are above a fixed threshold Θ, see Fig. 2B.

For the sake of simplicity, we assume a symmetric scenario with equal threshold Θ for both $s(x)$ and $f(x)$ for the two-morphogen growth rule. A more general case can be mapped to this special case by a simple rescaling. Source width (w) and position (x_0) are kept constant; more realistic scenarios of source growth are explored in the next section.

We numerically simulated morphogen dynamics according to Eq. (1) coupled with growth for the one- and two-morphogen growth rules introduced above, see Fig. 2. For both growth rules, the amplitudes of the morphogen gradients decrease as the system grows. Consequently, for the one-morphogen growth rule, the growth zone where morphogen levels exceed the threshold ($c(x,t) > \Theta$) shrinks at its border opposite to the source, until – for suitable parameter choices – growth eventually arrests (Fig. 2A). For the two-morphogen growth rule, the growth zone where the levels of both morphogens exceed the threshold ($s(x,t) > \Theta$ and $f(x,t) > \Theta$) shrinks even faster and at both borders, as the two opposing morphogen profiles overlap less when the system grows (Fig. 2B).

Fig. 2C and D show the final system size L^* at growth arrest for the one- and two-morphogen growth rule, respectively. For the one-morphogen growth rule, growth arrests only if the growth threshold Θ exceeds a critical

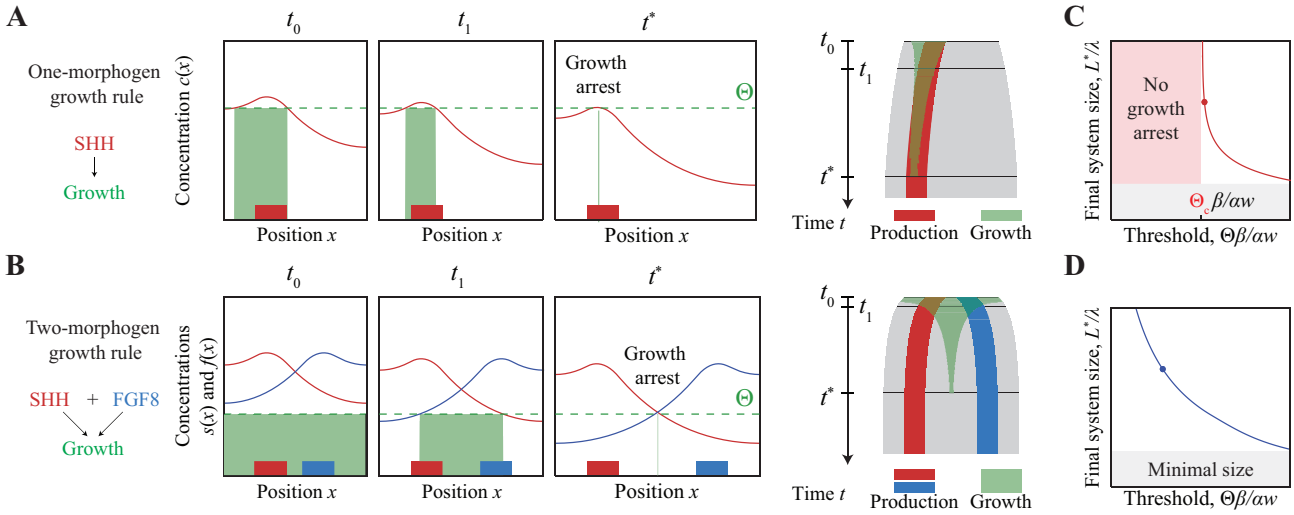

Figure 2. *Two putative growth rules. A.* Schematic of *one-morphogen growth rule*: the tissue grows where the concentration $c(x)$ of a single morphogen is above the growth threshold Θ. Morphogen source region (red region), morphogen gradient (red curve), growth threshold Θ (dashed green line), and growth zone (green region) at different time points. A corresponding kymograph of simulated tissue growth until growth arrest is shown to the right. *B.* Schematic of *two-morphogen growth rule*: a tissue grows only where the concentrations of both morphogens are above the growth threshold Θ. Morphogen gradients (red, blue) of the two morphogens at different time points, analogous to panel A. A kymograph shows production regions of both morphogens (red, blue). *C.* Final system size L^* normalized by pattern length-scale λ as function of a normalized growth threshold $\Theta\beta/\alpha w$ for the one-morphogen growth rule. Θ_c indicates the critical threshold below which the one-morphogen growth rule fails to arrest growth. *D.* Final system size L^* normalized by pattern length-scale λ as function of normalized growth threshold $\Theta\beta/\alpha w$ for the two-morphogen growth rule. Threshold parameter and final system size in panels A and B are indicated by a point in panels C and D, respectively.

value Θ_c, where $\Theta_c = \alpha w/(D\beta)^{1/2}$ for the limit case of a point source region (for details, see SI appendix, Eq. S28); for $\Theta < \Theta_c$, the system will grow indefinitely (Fig. 2C). For the two-morphogen growth rule, growth always arrests for any threshold (Fig. 2D). Since we consider a source with constant size and position, and the source region should fit into the system, the size of the system should be at least $w + x_0$, setting a minimal size. While we considered an idealized case where growth is slower than the dynamics of the morphogens, implying that morphogen gradients are always in quasi-steady state, numerical simulations reveal qualitatively similar behavior when this assumption is relaxed (SI appendix, Fig. S5). In the SI appendix, we also give analytic formulas for the final system size L^* as a function of the growth threshold Θ for the limit case of a point source region (Eqs. S27, S30). There, we also analyzed the sensitivity of the final system size L^* to the model parameters (Fig. S6), and found that the two-morphogen growth rule is less sensitive to parameter variations and ensures growth arrest for a wider range of parameters. This basic model shows that morphogen-dependent tissue growth can self-terminate, but does not include any scaling. Next, we investigate how tissues can attain the correct, proportionate final size through growth arrest in animals of different sizes.

Dynamic vs. static scaling of morphogen gradients

In the generic model of growth control from the preceding section, the final system size L^* only depends on the initially defined morphogen gradient parameters. In axolotl limb regeneration, the final limb size depends on animal size, suggesting that some parameters of morphogen gradients should be size-dependent. In an idealized scenario of *proportional growth*, the final size L^* of the system should be proportional to animal size L_a. Similarly, blastema size at the beginning of regeneration increases with animal size (Fig. 1C). Hence, in a simplified scenario, we assume that the initial system size L_0 is proportional to animal size L_a. To investigate how scaling of morphogen parameters could affect tissue growth, we investigate different scenarios for the size dependence of morphogen parameters.
We say that a morphogen gradient scales with a size ℓ if at least one of its features, source width w or pattern length-scale λ, both of which affect the signaling range, scales with this size ℓ. We distinguish two fundamentally different scaling scenarios, which differ by different interpretations of ℓ:

- *dynamic scaling* with growing blastema size $L(t)$, corresponding to the choice $\ell = L(t)$, and
- *static scaling* with animal size L_a, i.e. $\ell = L_a$.

For each of these two main scenarios, we consider three sub-scenarios. In all three sub-scenarios, we assume that the source region width and its position scale as $w \sim \ell$ and $x_0 \sim \ell$. In the first sub-scenario, which we term *source scaling*, the pattern length-scale λ is independent of size ℓ, see Fig. 3, left columns. In two additional sub-scenarios, in addition to source width, also the pattern length-scale scales as $\lambda \sim \ell$. According to Eq. 2, either the effective diffusion coefficient D or the morphogen degradation rate β must change with ℓ. This defines a second and third sub-scenario, which we refer to as D*-scaling* (i.e., $D \sim \ell^2$), and β*-scaling* ($\beta \sim \ell^{-2}$), respectively, see Fig. 3, middle and right columns. The three sub-scenarios affect gradient amplitude A in different ways (SI appendix, Table S2): A increases with increasing size ℓ for source scaling, and even more so for β-scaling, where in addition to scaling of the source also the degradation rate β decreases for larger ℓ. In the case of D-scaling, the amplitude A stays approximately constant, as the effects of the source scaling and of the increase in diffusion cancel each other. Dynamic scaling has been reported in several systems (20; 21; 22; 23; 24; 25; 26; 27), and shall therefore be analyzed first.

Dynamic scaling with blastema size. In the absence of scaling, both the one-morphogen and the two-morphogen growth rules enable growth arrest. If the morphogen gradients exhibit dynamic scaling, model parameters and thus morphogen concentrations change dynamically with the growing blastema size $L(t)$. For most scenarios of dynamic scaling, concentrations stay approximately constant or even increase, and hence growth does not arrest anymore, see Fig. 3A. The only exception is growth arrest for the special case when the pattern length-scale λ does not scale, and the two-morphogen rule is assumed. We obtain similar results without scaling of the source (SI appendix, Table S2). More generally, if either size w or position x_0 of the morphogen source scale, we obtain a combinatorial set of 32 sub-scenarios: growth arrests in 10 of these sub-scenarios for the two-morphogen growth rule, but only 4 sub-scenarios for the one-morphogen growth rule (SI appendix, Figs. S7-S9). However, even if growth arrests, the final system size L^* is independent of the initial system size L_0. Thus, in the case of dynamic scaling with growing blastema size, proportional growth is not possible.

Scaling with animal size. Next, we explore the scenario of scaling with animal size, where the parameters of the morphogen dynamics are set by the animal size L_a and then remain constant during blastema growth. This could occur if those parameters are set by systemic factors (e.g. hormonal or metabolic). As parameters of the morphogen dynamics remain constant during blastema growth, for animals of fixed size, the system behaves exactly the same way as in the case without scaling. We conclude that growth will arrest under minimal assumptions as described in Fig. 2. However, the final blastema size L^* now depends on the animal size L_a in a non-trivial manner, see Fig. 3D. Proportional growth with $L^* \sim L_a$ is obtained exactly for D-scaling. For β-scaling, L^* increases super-linearly with L_a. These predictions are robust, and we obtain similar results, e.g., in the limit case of a point source (SI appendix, Table S2). While Fig. 3 focused on the limit case of slow growth $g \ll \beta$, we observe virtually the same proportional growth for the two-morphogen growth rule (and variants thereof with graded growth response) if growth is fast (SI appendix, Fig. S5). Similarly, results virtually do not change if instead of the reflecting boundary conditions used in Fig. 3, we assume either open or absorbing boundary conditions, with the exception of the one-morphogen growth rule, which does not facilitate growth arrest for these alternative boundary conditions (SI appendix, Fig. S10). This, once more, highlights the robustness of the two-morphogen growth rule.

Combination of dynamic and static scaling. While Fig. 3C shows that dynamic scaling alone cannot ensure proportional growth, intriguingly, a combination of dynamic and static scaling can. For example, a scenario where all SHH parameters exhibit dynamic scaling and all FGF parameters exhibit static scaling ensures approximately proportional growth over a five-fold range of initial system sizes if D-scaling (i.e., size-dependent regulation of effective diffusion coefficients) is assumed (SI appendix, Fig. S11). This remains true even if all morphogen parameters – except FGF source size – exhibit dynamic scaling.

Quantification of size-dependent morphogen gradients

To assess putative scaling of morphogen gradients in regenerating axolotl limb blastema, we quantitatively analyzed SHH and FGF8 source regions in 3D in animals of different sizes and at several different regeneration time points. We used Hybridization Chain Reaction (HCR) RNA *in situ*, combined with tissue clearing and confocal microscopy to perform 3D quantitative measurements of SHH and FGF8 gradient parameters in developing limb buds and in regenerating limb blastemas from animals of three different sizes (snout-to-tail animal size: 3 cm, 5 cm, 7 cm). Measurements were taken at multiple time points (days post amputation, dpa) throughout the period when both signaling centers were present, see Fig. 4A. We first quantified blastema size along the line in 3D passing through SHH and FGF8 source region centers as in Fig. 1C, see Fig. 4B. Next, we quantified the linear sizes of SHH and FGF8 source regions by computing the cubic root of the volume enclosed by the 50%-iso-surfaces of the respective mRNA signals, which defines a length-scale that characterizes source size. We also quantified the gap size x_0 between the source regions and the tissue boundary corresponding to the source position. Finally, the

spatial range of FGF8 signaling was inferred from the volume enclosed by the 50%-iso-surface of *Dusp6* mRNA, a well-established downstream target of FGF8 signaling (28; 29; 30). All morphogen gradient parameters exhibit a clear size dependence. Yet, distinguishing dynamic and static scaling is complicated by the fact that blastema size and animal size are correlated (Fig. S2-S3). We first tested both a linear regression as a function of blastema size (left column in Fig 4D), and a linear regression as a function of animal size (right column). For both fit scenarios, we obtained satisfactory fits, with statistically significant size dependence, suggesting that both static and dynamic scaling may contribute to the observed size-dependent patterns. A contribution of dynamic scaling is suggested by the temporal increase of gradient parameters within some animal size groups, see SI appendix, Fig. S12. On the other hand, static scaling with animal size is compatible with the data, with R^2 values only slightly smaller or even larger than those of the linear regression against blastema size. To gain further insight, we performed a partial correlation analysis on this data, which allows testing for conditional statistical independence (SI appendix, Table S3): After factoring out the influence of animal size, less than 0.1% of the remaining variance of FGF8 source width w could be explained by blastema size, with no statistically significant correlation. In contrast, an analogous analysis for SHH source size revealed a much higher explained variance of 58% with high significance levels $p < 0.1\%$, indicative of a contribution of dynamic scaling for SHH. The statistical analysis for the other morphogen parameters suggests different contributions of static and dynamic scaling, see Fig. 4D and SI appendix. In conclusion, the data for the FGF8 source region and possibly other morphogen gradient parameters is compatible with static scaling. Note that in our model, it is sufficient if only a subset of morphogen parameters, e.g. only FGF8 source size, exhibit static but not dynamic scaling, to ensure growth arrest and proportional growth (SI appendix, Fig. S11).

Mutual feedback between morphogens

Previous works suggested a mutual feedback between SHH and FGF production (13; 14; 15). Above, we assumed that both morphogens are produced independently of each other and their source regions and production rates remain constant during tissue growth without specifying biological mechanisms of maintaining morphogen production. Here, we theoretically describe a possible minimal feedback scenario. We assume that there are regions competent for SHH or FGF8 production (shown as transparent regions in Fig. 5A). This assumption is supported by distinct properties of anterior and posterior blastema regions (16; 31; 32; 33). We further assume that SHH and FGF8 are produced in their respective competent region if the opposite morphogen concentration is above a feedback threshold Θ_{fb}. With such mutual feedback, the system can be in one of two limiting regimes, depending on the relative magnitude of the growth threshold Θ and the feedback threshold Θ_{fb}. In the first regime, growth arrests because the growth threshold is reached first (green region in Fig. 5B). The system thus behaves similar to the case without feedback described above and arrests growth, while morphogen production in still ON. In the second regime, the feedback threshold is reached first (orange region in Fig. 5B). As a consequence, the source regions of morphogen production shrink rapidly, and morphogen production is switched OFF. Without morphogen production, also tissue growth arrests. In this second regime, the feedback between the two morphogens functions as a tissue-level ON/OFF switch for growth. While Fig. 5B shows results for the two-morphogen growth rule, the system behaves qualitatively similarly for the one-morphogen growth rule. Signaling delays of morphogen feedback would result in a gradual decrease of morphogen profile amplitudes, but otherwise similar behavior.
Adding feedback to the system thus does not significantly change its behavior with regard to growth arrest, demonstrating that our conclusions remain applicable also in a more realistic model. Feedback between the two morphogens could be a means of avoiding the slow fade-out of growth observed without feedback (Fig. 2), or even of switching off growth homogeneously throughout the system.

Discussion

Inspired by the size-adaptive regeneration of axolotl limbs, we addressed the general question of how morphogen-dependent tissue growth can be arrested once a tissue has reached its correct size. In our prototypical minimal model, tissue growth is induced by a threshold rule for either a single morphogen, or a pair of oppositely-oriented morphogen gradients. The two-morphogen growth rule with two oppositely-oriented gradients provides a particularly robust mechanism of growth arrest: the overlap between the two gradients induces growth; this growth increases the spatial separation between the two morphogen sources and thus decreases the overlap between the two gradients. This negative feedback loop robustly terminates growth at a specific tissue size. Proportional growth, however, where the final system size is proportional to initial size, requires scaling of morphogen gradients. We distinguished two fundamental scaling scenarios: *dynamic scaling* of morphogen gradients with the growing blastema, or *static scaling*, where morphogen gradient parameters depend on animal size, but remain constant during growth. Our theoretical analysis shows that static scaling with animal size of at least a subset of morphogen parameters is necessary and sufficient for proportional growth if a switch-like growth rule is assumed (Fig. 3 and Fig. S11 in SI appendix). We expect similar results for graded growth responses (Fig. S5).

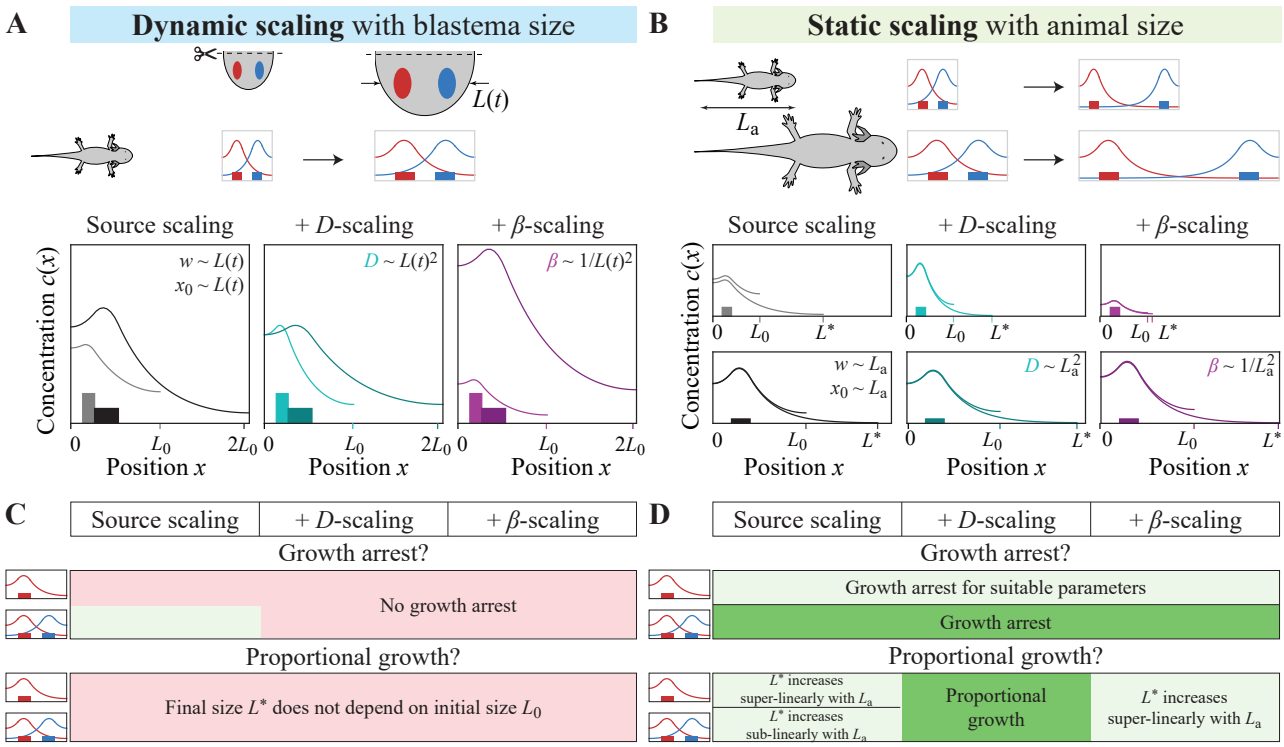

Figure 3. *Two scenarios of morphogen gradient scaling.* *A.* Schematic of *dynamic scaling*: morphogen gradients scale with growing blastema size $L(t)$. Different sub-scenarios of dynamic scaling affect the amplitude of morphogen gradients differently (source scaling with production rate $\alpha \sim L(t)$: black, D-scaling with effective diffusion coefficient $D \sim L(t)^2$: cyan, β-scaling with degradation rate $\beta \sim 1/L(t)^2$: magenta), see text for details. For each sub-scenario, source regions (boxes) and morphogen profiles (solid lines) are shown for initial tissue size L_0 and when tissue size has doubled in lighter and darker color, respectively. *B.* Schematic of *static scaling* with animal size: parameters of morphogen dynamics depend on animal size, but remain constant during growth. Same sub-scenarios of scaling as in panel A, but parameters of morphogen dynamics now depend on animal size L_a. Shown are morphogen gradients at the beginning of growth with initial system size L_0 (assumed proportional to L_a for simplicity) and at growth arrest with final system size L^* for two values of L_0 (upper and lower row). *C.* Summary of modeling predictions for *dynamic scaling* with blastema size, corresponding to the three scaling sub-scenarios introduced in panel A. For *dynamics scaling*, growth arrests for any growth threshold Θ for the two-morphogen growth rule if the morphogen source scales, but not the pattern length-scale λ, but not for any other sub-scenario. However, even in the scenario with growth arrest, the final system size L^* is independent of initial system size, i.e. there is no proportional growth. *D.* Summary of modeling predictions for *static scaling* with animal size, corresponding to the three scaling sub-scenarios introduced in panel B. For static scaling, morphogen dynamics parameters remain constant during growth. Correspondingly, growth arrests for any growth threshold Θ for the two-morphogen growth rule (introduced in Fig. 2), yet for the one-morphogen rule only if the growth threshold Θ exceeds a critical value Θ_c. Proportional growth is achieved for the D-scaling sub-scenario, where both the effective diffusion coefficient D and the source region scales with animal size.

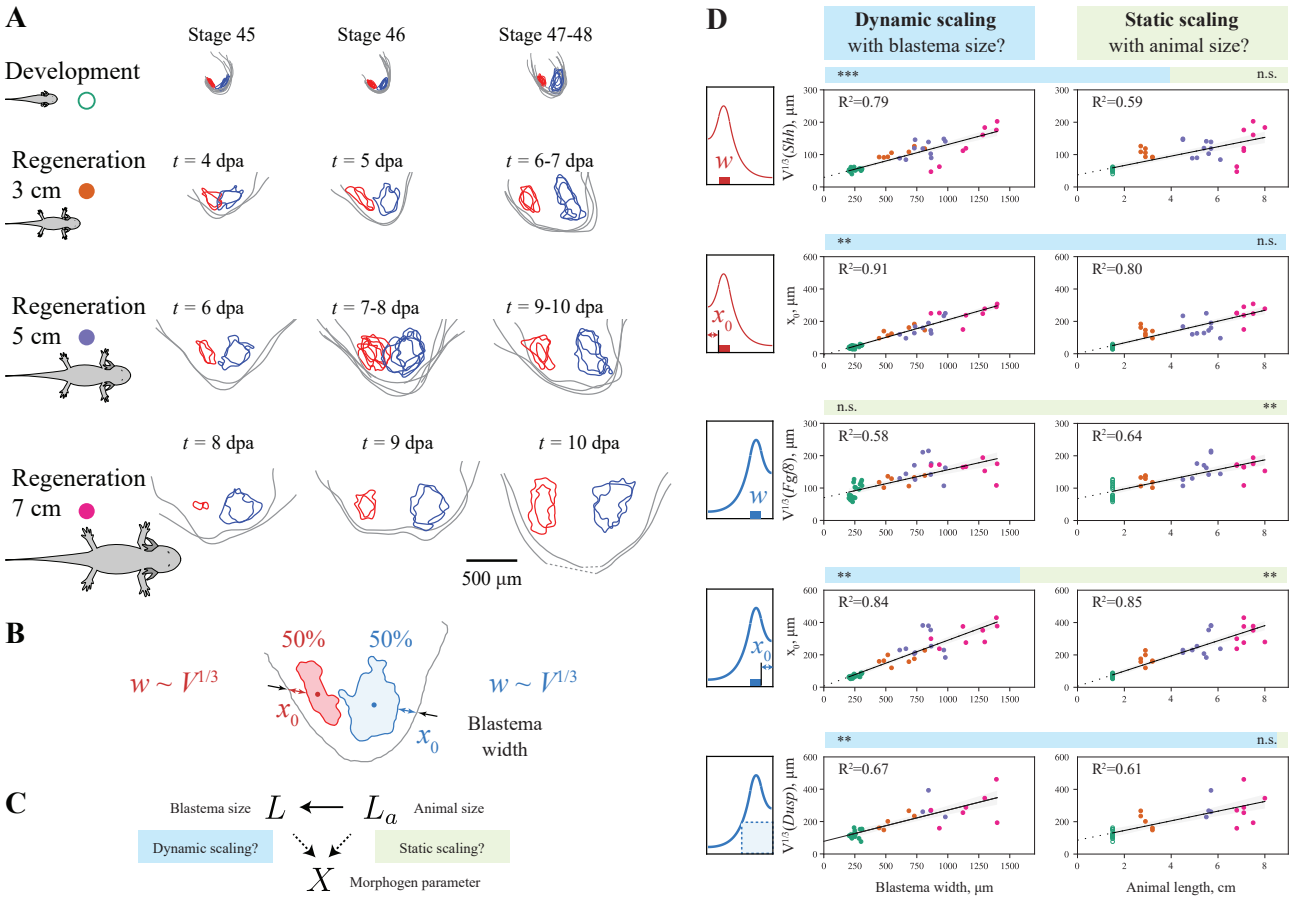

Figure 4. *Size-dependence of SHH and FGF8 morphogen gradients. A.* Outlines of SHH and FGF8 source regions from *in situ* hybridization in limb buds at different developmental stages, as well as regenerating blastemas of different-sized animals and at different regeneration time points (*Shh*: red, *Fgf8*: blue, 50% threshold of normalized intensity, shown as binary projections along dorsal-ventral axis on plane containing the centers of the *Shh* and *Fgf8* regions, see SI appendix for details; by convention, italicized names, e.g. *Shh* and *Fgf8*, refer to mRNA, indicating morphogen production, while capitalized names, e.g. SHH and FGF8, refer to the corresponding proteins. *B.* Definition of morphogen parameters: the linear source size $V^{1/3}$ determined from 3D-volume V enclosed by 50%-iso-surface for *Shh* defines the source width w for SHH, the gap size between SHH source boundary and tissue boundary defines the source position x_0 (measured in 2D-projections along a line connecting the centers of the *Shh* and *Fgf8* regions as shown in panel A); analogous definitions for *Fgf8*. We determined a proxy for the FGF8 signaling range as $V^{1/3}$ from the 3D-volume V enclosed by the 50%-iso-surface of the FGF8 target *Dusp6*. *C.* A morphogen parameter X may exhibit either *dynamic scaling* with blastema size L, or *static scaling* with animal size L_a. Since L and L_a are correlated, causal inference is needed to test these scenarios. *D.* Morphogen parameters as defined in panel B as function of blastema width (left column) and animal length (right column). Colors represent animal size as in panel A and Fig. 1C (filled circles: regeneration, open green circles: development; linear regression: black). For each morphogen parameter, a bar plot represents the result of a partial correlation analysis (statistical significance and proportion of residual variance from a test for the respective opposite null hypothesis, indicative of dynamic scaling (blue, null hypothesis: only static scaling), and static scaling (green, null hypothesis: only dynamic scaling), see SI appendix D for details).

Blastema growth in axolotl regeneration is more complex. Our analysis addresses only the first stage of blastema outgrowth, which is followed by cell differentiation and a second growth phase. The second phase, which is independent of SHH-FGF signaling, is thought to be regulated by neuronal signals (7). Nevertheless, the first growth phase and the blastema size at the onset of tissue differentiation is important to ensure accurate limb patterning, including the correct number of bone elements. Interestingly, blastema growth is not proportional to limb size in very large animals ($\gtrsim$ 10 cm) and is more accurately described by allometric scaling laws (8) (confirmed also in SI appendix, Fig. S2). This suggests limits of scaling. Note that sub-scenarios of our model can reproduce allometric scaling laws as observed experimentally (Fig. S5 in SI appendix). While our minimal model showed that exclusively dynamic scaling cannot enable proportional growth, it is likely that a combination of dynamic and static scaling applies in axolotl. Furthermore, dynamic scaling could still be compatible with proportional blastema growth if a separate timer mechanism terminates growth after a fixed time.

We used *in situ* hybridization in 3D tissues to quantify SHH and FGF8 source regions and FGF8 signaling

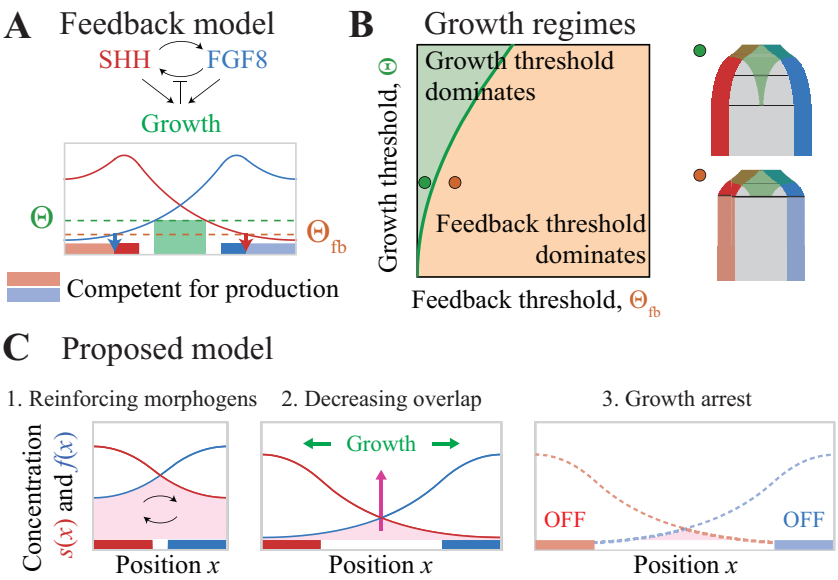

Figure 5. *Feedback model of reinforcing morphogens.* *A.* Minimal model of mutual feedback between oppositely-oriented morphogen gradients: Each morphogen can only be produced in a region of competent cells (transparent red and blue bars) where the concentration of the respective other morphogen exceeds a threshold (Θ_{fb}, orange dashed), defining two source regions (solid red and blue bars). *B.* Phase diagram of growth regimes as a function of growth threshold Θ and feedback threshold Θ_{fb}, here shown for the two-morphogen growth rule, exhibiting two regimes: the growth threshold Θ dominates, resulting in dynamics analogous to the case without feedback (green) as in Fig. 2, or, the feedback threshold Θ_{fb} dominates, resulting in instantaneous and homogeneous growth arrest across the entire system (orange). *C.* Model of growth arrest by the growth-threshold regime: 1. The tissue grows (green) where both morphogens (red and blue) are above the growth threshold (green dashed). 2. Tissue growth pushes the two morphogen sources apart, thus decreasing the region where the two morphogens overlap. 3. Due to the mutual feedback between the two morphogens, their respective source regions start shrinking rapidly, switching off both morphogens and arresting growth.

range in developing limb buds and regenerating blastemas of different sizes at different time points. We find a clear size-dependence of morphogen gradient parameters. In particular, our data suggests static scaling with animal size for the FGF8 source region size, while the SHH source region size may exhibit dynamic scaling. This extends the recently published *in situ* hybridization analysis of source sizes in tissue slices for a single morphological stage in (8). Our analysis of growth control by scaling morphogen gradients is independent of the particular implementation of morphogen scaling, and only depends on which parameters of morphogen dynamics are adjusted in a size-dependent manner. Scaling of morphogen gradients has been reported in a number of systems (20; 21; 22; 23; 24; 25; 26; 27). A common concept in proposed mechanisms is the presence of a modulator such as an "expander", whose concentration regulates, e.g., the effective diffusion coefficient or degradation rate of a morphogen (34; 35; 36; 37). In expander-dilution models, tissue growth dilutes the concentration of the expander inversely proportional to tissue volume (38). In expander-repression models, the production of the expander depends on the morphogen itself (34). Recently, SCUBE family molecules were shown to affect SHH spreading (39) and suggested to act by an expansion-repression mechanism to control the amplitude and pattern length-scale of the SHH gradient in the zebrafish neural tube (40), compatible with a mechanism of D-scaling.

SHH and FGF8 also guide limb development in other vertebrates (2; 3). This pair of morphogen gradients must be switched on, but later also switched off again. Previous mathematical models focused on the temporal dynamics of morphogens (15), including the role of intermediate morphogens Bone Morphogenetic Protein (BMP) and Gremlin (GREM), which itself are thought to be a part of the SHH-FGF feedback loop. To explain how SHH and FGF become switched off again, various hypotheses reviewed in (41) were put forward: A first hypothesis suggests that the medial portion of the SHH competent region, which previously expressed SHH, loses this competence, creating an expanding region of cells that are not competent to express either SHH or GREM or FGF8 (42). A second hypothesis suggests that FGF8 terminates GREM in a concentration-dependent manner (43); alternatively, a low concentration of BMP could activate GREM at early stages, while a higher concentration of BMP could suppress GREM later (44). We comment that these hypotheses would require signal delays to prevent becoming trapped in an intermediate state between "on" and "off". Another hypothesis would be a timer mechanism that switches off SHH and FGF after a preset growth period (45). These hypotheses not only underline the intricate molecular interactions involved in the growth control of developing and regenerating limbs but also start to appreciate the importance of spatial patterns of

signaling.

Our model proposes that a coupling of spatial patterns and growth provides a simple and robust mechanism by which the SHH-FGF feedback loop could become switched off after the first stage of blastema outgrowth is completed (Fig. 5C). Our minimal model suggests specific experiments. Quantifying SHH and FGF8 morphogen gradients as function of animal size and time, ideally by measuring protein concentrations instead of down-stream signaling, will allow testing our theory prediction of static scaling with animal size (or limb size). Cell culture experiments with controlled levels of morphogens as initiated in (8) could test the growth rules proposed here. This could pave the road towards more realistic, data-driven models that capitalize on the concepts laid out in the idealized, one-dimensional model studied here. In conclusion, we proposed a simple mechanism of two opposing morphogen gradients that reinforce each other, to enable robust growth arrest and proportional tissue growth by scaling of morphogen parameters with animal size.

Methods

Numerical methods

In the presence of tissue growth with local growth rate $g(x,t)$, Eq. (1) changes to

$$\partial_t c(x,t) = D\,\partial_x^2 c - v(x,t)\partial_x c - [\beta + g(x,t)]c + \alpha\,\chi_{w(t)}(x) \quad , \tag{4}$$

where $\partial_x v = g$ (21; 46). This equation is numerically solved using a modified Euler scheme in a Lagrangian frame with non-uniform spatial grid, whose bin sizes Δx_i are updated according to $\Delta x_i(t_{n+1}) = [1 + g(x_i,t_n)\Delta t]\Delta x_i(t_n)$.

Whole-mount HCR *in situ* hybridization and imaging

Shh, *Fgf8* and *Dusp6* mRNAs were detected in formaldehyde-fixed limb blastema and developing limb buds obtained from different-sized animals at different timepoints by whole mount HCR, a fluorescent RNA *in situ* method as described in (47) with minor modifications, followed by refractive index matching and confocal imaging in 3D (for detailed protocol, see SI appendix).

Image analysis

For analysis of 3D multi-channel z-stack images, blastemas were segmented using APOC (48) trained with user-specified ground truth labels applied to the *Shh* channel using Napari (49) and custom Python code. Blood vessels detected in the autofluorescence channel were segmented using APOC, and the corresponding binary mask was excluded from all channels. The linear size of SHH and FGF8 source regions, as well as of FGF8 signaling indicated by *Dusp6* mRNA, were determined as the cubic roots of the volumes enclosed by the respective 50%-iso-intensity surfaces (after denoising and min-max normalization of each channel). Blastema size was measured in 3D images along a line passing through the centers of the *Shh* and *Fgf8* regions. Gap sizes between the blastema boundary and the boundaries of these source regions (x_0) were measured along the same line, yet using 2D-projections to account for a possible non-convex shape of source regions.

Data, Materials and Software Availability

Raw image data and Python code for growth simulations and image analysis can be accessed at a public github repository at https://github.com/NataliaLyubaykina/axolotl_limb_regeneration_s. All other data, methods and analyses are included in the main text or in SI appendix.

Acknowledgements

We thank Leo Otsuki and Elly M. Tanaka (IMBA) for the transgenic axolotl line (tgSceI(ZRS:TFPnls-T2A-ERT2-Cre-ERT2)^{Etnka}. We thank Elly M. Tanaka, as well as all members of the Sandoval-Guzmán and Friedrich groups for stimulating discussions, the animal carers of the CRTD (Beate Gruhl and Anja Wagner) for dedicated axolotl care, the light microscopy facility of the CMCB for excellent support, as well as Veikko F. Geyer for statistical analysis support. TSG and BMF acknowledge funding from a joint D-A-CH grant from the German and Austrian Science Foundations (441649267, jointly with Elly M. Tanaka). BMF was additionally supported by the Deutsche Forschungsgemeinschaft (DFG, German Research Foundation) under Germany's Excellence Strategy - EXC-2068-390729961, as well as through a Heisenberg grant (421143374).

References

1. Simon A, Tanaka E (2013) Limb regeneration. *Wiley Interdisciplinary Reviews: Developmental Biology* 2(2):291–300.
2. Muneoka K, Bryant SV (1982) Evidence that patterning mechanisms in developing and regenerating limbs are the same. *Nature* 298(5872):369–371.
3. Payzin-Dogru D, Whited JL (2018) An integrative framework for salamander and mouse limb regeneration. *The International Journal of Developmental Biology* 62(6-7-8):393–402.
4. Young JJ, Tabin CJ (2017) Saunders's framework for understanding limb development as a platform for investigating limb evolution. *Developmental Biology* 429(2):401–408.
5. Vieira WA, Wells KM, McCusker CD (2020) Advancements to the axolotl model for regeneration and aging. *Gerontology* 66(3):212–222.
6. Leigh ND, Currie JD (2022) Rebuilding limbs, one cell at a time. *Developmental Dynamics* 251(9):1389.
7. Wells KM, Kelley K, Baumel M, Vieira WA, McCusker CD (2021) Neural control of growth and size in the axolotl limb regenerate. *eLife* 10:e68584.
8. Furukawa S, Yamamoto S, Ohashi A, Morishita Y, Satoh A (2024) Allometry in limb regeneration and scale-invariant patterning as the basis of normal morphogenesis from different sizes of blastemas. *Development* pp. dev–202697.
9. Torok MA, Gardiner DM, Izpisúa-Belmonte JC, Bryant SV (1999) Sonic hedgehog (SHH) expression in developing and regenerating axolotl limbs. *Journal of Experimental Zoology* 284(2):197–206.
10. Tickle C, Towers M (2017) Sonic hedgehog signaling in limb development. *Frontiers in Cell and Developmental Biology* 5:14.
11. Han MJ, An JY, Kim WS (2001) Expression patterns of FGF-8 during development and limb regeneration of the axolotl. *Developmental Dynamics* 220(1):40–48.
12. Purushothaman S, Elewa A, Seifert AW (2019) FGF-signaling is compartmentalized within the mesenchyme and controls proliferation during salamander limb development. *eLife* 8:e48507.
13. Laufer E, Nelson CE, Johnson RL, Morgan BA, Tabin C (1994) Sonic hedgehog and FGF-4 act through a signaling cascade and feedback loop to integrate growth and patterning of the developing limb bud. *Cell* 79(6):993–1003.
14. Niswander L, Jeffrey S, Martin GR, Tickle C (1994) A positive feedback loop coordinates growth and patterning in the vertebrate limb. *Nature* 371(6498):609–612.
15. Bénazet JD, et al. (2009) A self-regulatory system of interlinked signaling feedback loops controls mouse limb patterning. *Science* 323(5917):1050–1053.
16. Otsuki L, Plattner S, Taniguchi-Sugiura Y, Falcon F, Tanaka E (2025) Molecular basis of positional memory in limb regeneration. *Nature*.
17. Nacu E, Gromberg E, Oliveira CR, Drechsel D, Tanaka EM (2016) FGF8 and SHH substitute for anterior–posterior tissue interactions to induce limb regeneration. *Nature* 533(7603):407–410.
18. Glotzer GL, Tardivo P, Tanaka EM (2022) Canonical Wnt signaling and the regulation of divergent mesenchymal FGF8 expression in axolotl limb development and regeneration. *eLife* 11:e79762.
19. Wolpert L (1969) Positional information and the spatial pattern of cellular differentiation. *Journal of Theoretical Biology* 25(1):1–47.
20. Ben-Zvi D, Pyrowolakis G, Barkai N, Shilo BZ (2011) Expansion-repression mechanism for scaling the DPP activation gradient in *Drosophila* wing imaginal discs. *Current Biology* 21(16):1391–1396.
21. Wartlick O, et al. (2011) Dynamics of DPP signaling and proliferation control. *Science* 331(6021):1154–1159.
22. Stückemann T, et al. (2017) Antagonistic self-organizing patterning systems control maintenance and regeneration of the anteroposterior axis in planarians. *Developmental Cell* 40(3):248–263.
23. Mateus R, et al. (2020) BMP signaling gradient scaling in the zebrafish pectoral fin. *Cell reports* 30(12):4292–4302.
24. Romanova-Michaelides M, et al. (2022) Morphogen gradient scaling by recycling of intracellular DPP. *Nature* 602(7896):287–293.
25. Kicheva A, Briscoe J (2023) Control of tissue development by morphogens. *Annual Review of Cell and Developmental Biology* 39(1):91–121.
26. Nikolić M, et al. (2024) Scale invariance in early embryonic development. *Proc. Natl. Acad. Sci. U.S.A.* 121(46):e2403265121.
27. Rich A, et al. (2025) Decaying and expanding ERK gradients process memory of skeletal size during zebrafish fin regeneration. *bioRxiv* pp. 2025–01.
28. Molina GA, Watkins SC, Tsang M (2007) Generation of FGF reporter transgenic zebrafish and their utility in chemical screens. *BMC developmental biology* 7:1–14.
29. Li C, Scott DA, Hatch E, Tian X, Mansour SL (2007) Dusp6 (Mkp3) is a negative feedback regulator of FGF-stimulated ERK signaling during mouse development. *Development* 134(1):167–176.
30. Ekerot M, et al. (2008) Negative-feedback regulation of FGF signalling by DUSP6/MKP-3 is driven by ERK1/2 and mediated by Ets factor binding to a conserved site within the DUSP6/MKP-3 gene promoter. *Biochemical Journal* 412(2):287–298.
31. Carlson BM (1975) The effects of rotation and positional change of stump tissues upon morphogenesis of the regenerating axolotl limb. *Developmental Biology* 47(2):269–291.
32. Endo T, Bryant SV, Gardiner DM (2004) A stepwise model system for limb regeneration. *Developmental Biology* 270(1):135–145.
33. Bryant SV (1976) Regenerative failure of double half limbs in *Notophthalmus viridescens*. *Nature* 263(5579):676–679.
34. Ben-Zvi D, Barkai N (2010) Scaling of morphogen gradients by an expansion-repression integral feedback control. *Proc. Natl. Acad. Sci. U.S.A.* 107(15):6924–6929.
35. Werner S, et al. (2015) Scaling and regeneration of self-organized patterns. *Physical Review Letters* 114(13):138101.
36. Umulis DM, Othmer HG (2013) Mechanisms of scaling in pattern formation. *Development* 140(24):4830–4843.
37. Shilo BZ, Barkai N (2017) Buffering global variability of morphogen gradients. *Developmental Cell* 40(5):429–438.
38. Wartlick O, Mumcu P, Jülicher F, Gonzalez-Gaitan M (2011) Understanding morphogenetic growth control—lessons from flies. *Nature Reviews Molecular Cell Biology* 12(9):594–604.
39. Schlissel G, Meziane M, Narducci D, Hansen AS, Li P (2024) Diffusion barriers imposed by tissue topology shape hedgehog

morphogen gradients. *Proc. Natl. Acad. Sci. U.S.A.* 121(36):e2400677121.
40. Collins ZM, Ishimatsu K, Tsai TY, Megason SG (2023) A Scube2-SHH feedback loop links morphogen release to morphogen signaling to enable scale invariant patterning of the ventral neural tube. *bioRxiv* https://doi.org/10.1101/469239.
41. Zuniga A, Zeller R (2020) Dynamic and self-regulatory interactions among gene regulatory networks control vertebrate limb bud morphogenesis. *Current Topics in Developmental Biology* 139:61–88.
42. Scherz PJ, Harfe BD, McMahon AP, Tabin CJ (2004) The limb bud SHH-FGF feedback loop is terminated by expansion of former ZPA cells. *Science* 305(5682):396–399.
43. Verheyden JM, Sun X (2008) An FGF/Gremlin inhibitory feedback loop triggers termination of limb bud outgrowth. *Nature* 454(7204):638–641.
44. Nissim S, Hasso SM, Fallon JF, Tabin CJ (2006) Regulation of Gremlin expression in the posterior limb bud. *Developmental Biology* 299(1):12–21.
45. Saiz-Lopez P, et al. (2015) An intrinsic timer specifies distal structures of the vertebrate limb. *Nature communications* 6(1):8108.
46. Aguilar-Hidalgo D, et al. (2018) Critical point in self-organized tissue growth. *Physical Review Letters* 120(19):198102.
47. Choi HM, et al. (2018) Third-generation *in situ* hybridization chain reaction: multiplexed, quantitative, sensitive, versatile, robust. *Development* 145(12):dev165753.
48. Haase R, Lee D, Pop DD, Žigutytė L (2023) napari-accelerated-pixel-and-object-classification: 0.14.1. *https://doi.org/10.5281/zenodo.10071078*.
49. Chiu CL, Clack N, et al. (2022) Napari: a Python multi-dimensional image viewer platform for the research community. *Microscopy and Microanalysis* 28(S1):1576–1577.

Supporting Information for

Static morphogen scaling enables proportional growth in tissue growth model inspired by axolotl limb regeneration

Natalia Lyubaykina, Dunja Knapp, Pietro Tardivo, Maximilian Kotz, Tatiana Sandoval-Guzmán, Benjamin M. Friedrich

This PDF file includes:

1. Figures S1 to S12
2. Tables S1 to S3
3. Supplementary Methods
4. Supplementary Information for Mathematical Modeling

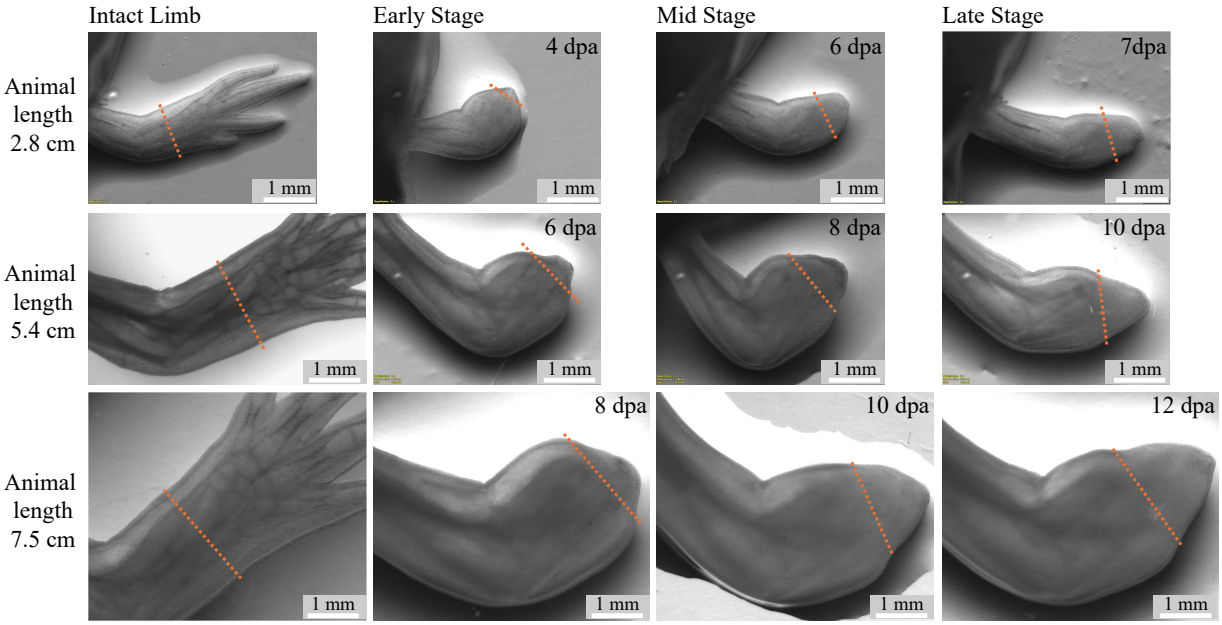

Figure S1. *Regeneration time-course in animals of three different sizes as used for the quantification of morphogen parameters.* Intact limbs and three analogous stages of regeneration (early, middle and late blastema stages) are shown for animals of different sizes: 2.8 cm, 5.4 cm and 7.5 cm length from snout to tail. Analogous time points were designated based on morphology and SHH and FGF8 morphogen dynamics. The orange dotted lines indicate the amputation plane. Days post amputation (dpa) are indicated. Early stage: initial cohort of undifferentiated cells accumulated underneath the wound epidermis and onset of SHH and FGF8 expression, mid-stage: fast-growing blastema, FGF8 expressed in a single contiguous cloud, late stage: blastema began to flatten along the dorso-ventral axis, FGF8 source region begins to split into dorsal and ventral cloud.

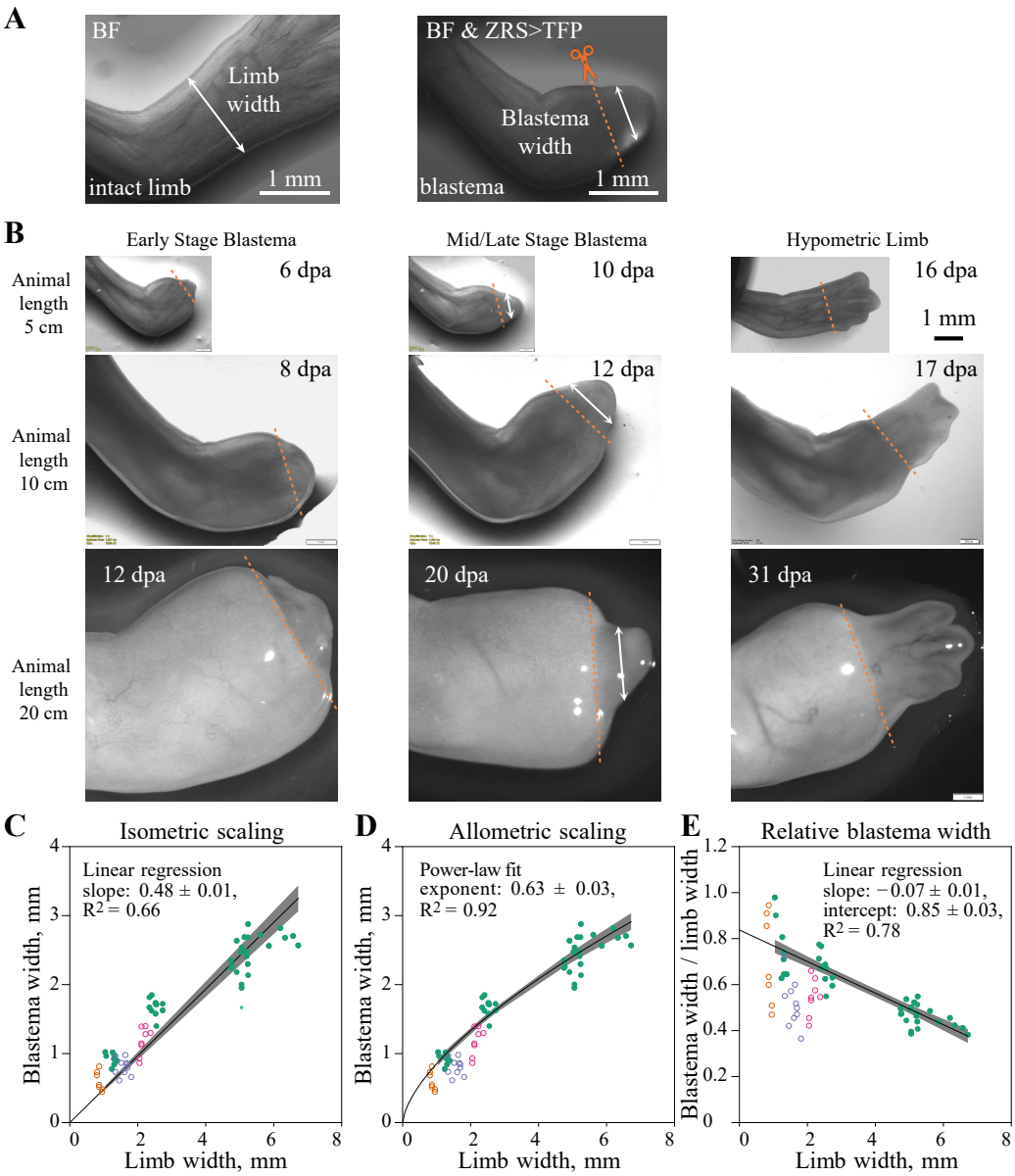

Figure S2. *Measurements of blastema width.* *A.* Schematic of limb width and blastema width measurements from wide-field images. White double arrows indicate the position of the limb/blastema width measurement, the orange dotted line the amputation plane. Specifically, the position and direction of limb width measurement was chosen to match the later amputation plane. The position of blastema width measurement was chosen as the center of the ZRS>TFP reporter expression, with measurement direction parallel to the amputation plane. *B.* Representative images of blastema in different-sized animals at different time points of regeneration. The amputation plane (i.e., the putative edge of blastema, orange dotted lines) and position of the blastema width measurements (white double arrows) are shown. The discrepancy between hypometric limb width and limb stump width (indicative of initial limb width) is more pronounced in larger animals. *C.* Mid/late-stage blastema width as a function of limb width (green filled symbols), together with proportional fit corresponding to an isometric scaling relation. *D.* Same data as in panel C, but with power-law fit corresponding to an allometric scaling relation. The width of mid/late-stage blastemas scales with exponent 0.63 ± 0.03 with intact limb width. Using the fact that the intact limb size scales with animal length with exponent 0.92 ± 0.01 (Fig. S3C), we conclude that blastema width scales with animal length with exponent $0.63 * 0.92 = 0.58 \sim 0.6$. *E.* The relative blastema width decreases as a function of limb width (and thus animal size). For comparison, blastema width as shown in Fig. 1C measured for different stages of blastema growth along a line connecting the centers of SHH and FGF8 source regions is shown as open symbols for 3-cm animal at 4-7 dpa (orange), 5-cm animal at 6-10 dpa (blue), 7-cm animal at 8-12 dpa (magenta). Here, we used the linear regression from Fig. S3B to relate animal length and limb width. Note that variability in determining the line connecting the centers of SHH and FGF8 source regions adds to the variability of these blastema width measurements. The corresponding data points were not used for the fits of allometric scaling relations shown. Data: Supplementary Data File Data_S1.xlsx.

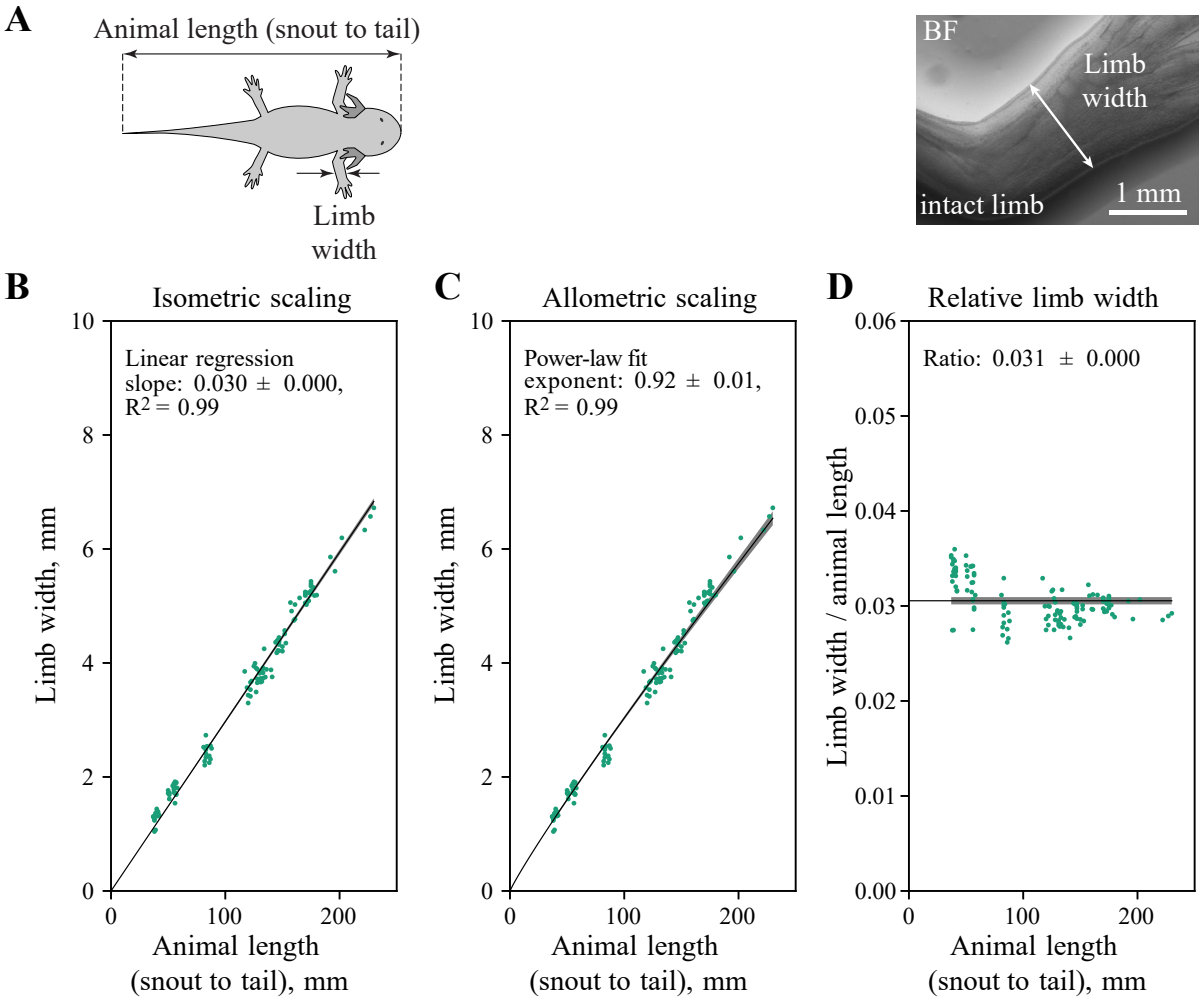

Figure S3. *Measurements of animal length and limb width. A.* Schematics of animal length measurements (from snout to tail) and limb width measurements from wide-field images; the white double arrow indicates the position of the limb width measurement. *B.* Limb width as a function of animal length, together with proportional fit corresponding to an isometric scaling relation. *C.* Same data as in panel A, but with power-law fit corresponding to an allometric scaling relation. *D.* The relative limb width stays approximately constant as a function of animal length. An analogous analysis using snout-to-cloaca length as alternative measure for animal size gave analogous results. Data: Supplementary Data File Data_S1.xlsx.

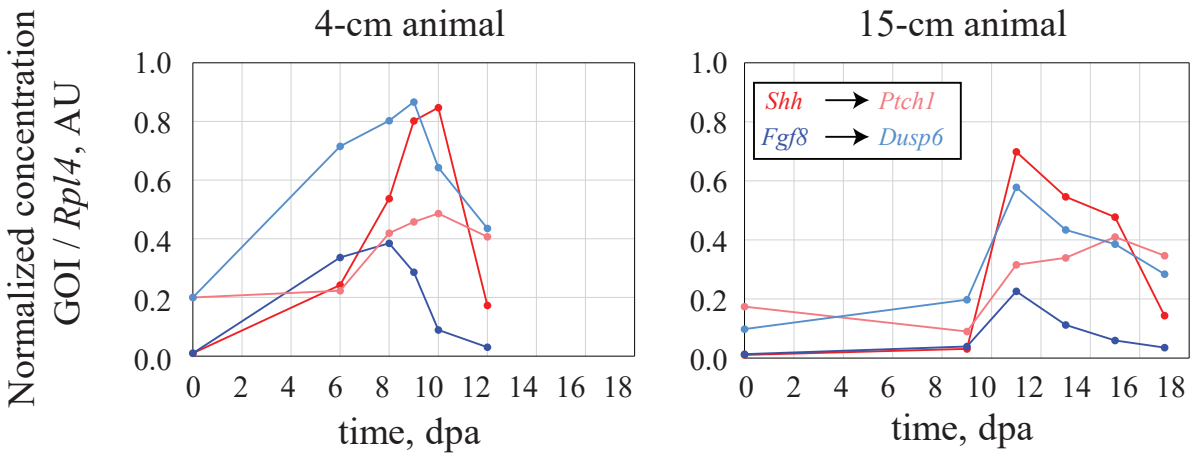

Figure S4. *Quantitative PCR (qPCR) analysis of Shh, Fgf8, and their downstream targets Ptch1 and Dusp6 during regeneration in animals of two different sizes (snout-to-tail length).* Experimentally measured mRNA values for each Gene of Interest (GOI) were normalized to the housekeeping gene *Rpl4* and presented in arbitrary units. The data represent mean values from two independent experiments. The approximately equal amplitudes of normalized *Shh* and *Fgf8* expression, together with the size-scaling of source regions shown in Fig. 4D, is consistent with the assumption of a size-independent morphogen production rate constant (parameter α in the model).

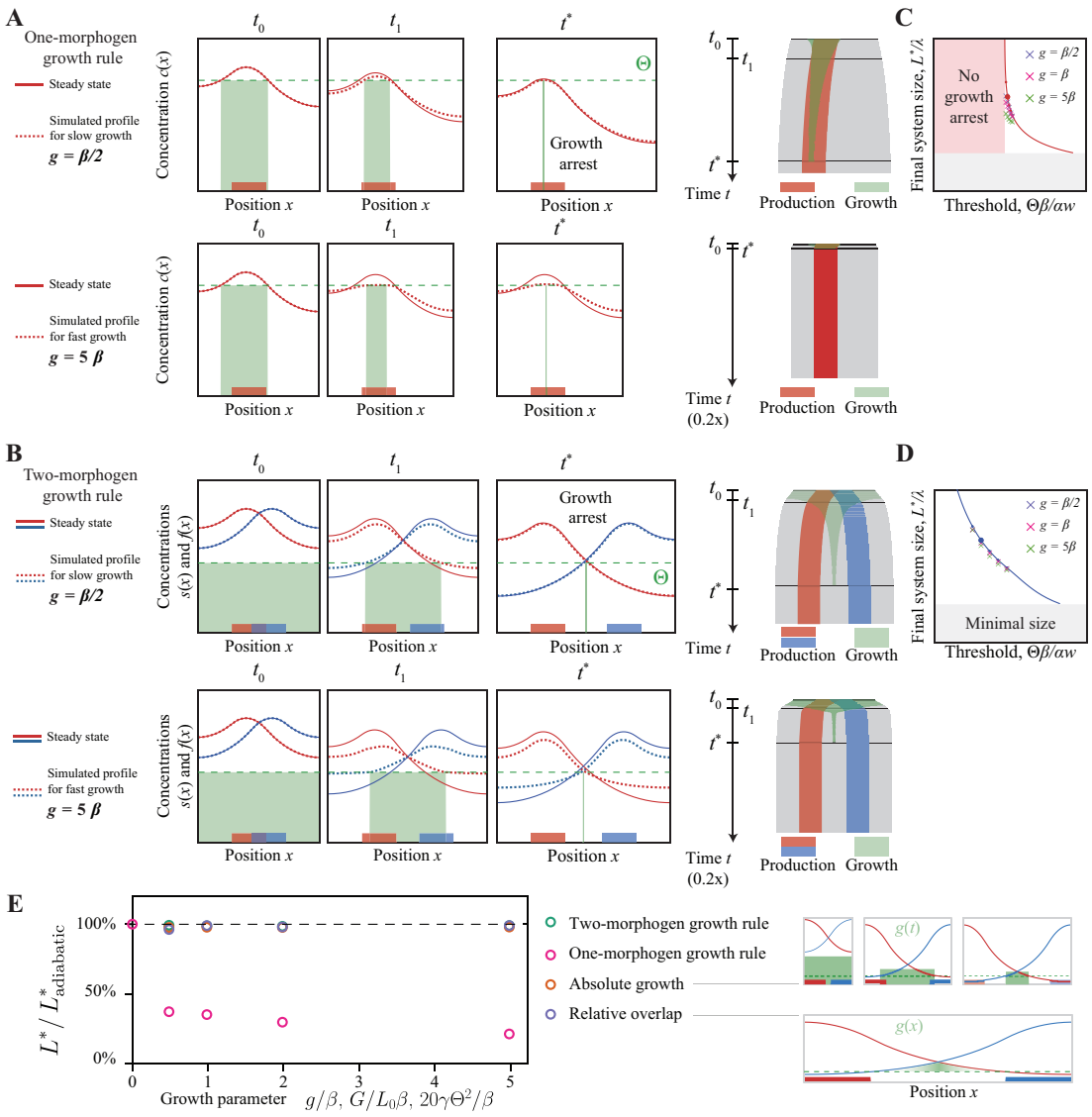

Figure S5. *Effect of the fast growth on final tissue size.* *A.* Morphogen source region (red region), morphogen gradient (red curve), growth threshold Θ (dashed green line), and growth zone (green region) at different time points for the one-morphogen growth rule analogous to Fig. 2A, yet for high growth rate g, resulting in non-steady-state concentration profiles. Dashed lines show morphogen profiles computed for the case of a finite growth rate g for two values of g (upper and lower panel, respectively), solid lines show morphogen profiles in the limit case of slow growth $g \ll \beta$ as considered in Fig. 2A. Corresponding kymographs of computed tissue growth analogous to Fig. 2A are shown to the right. *B.* Morphogen source region (red region), morphogen gradient (red curve), growth threshold Θ (dashed green line), and growth zone (green region) at different time points for the two-morphogen growth rule analogous to Fig. 2B, for a finite growth rate g. As in panel S5A, dashed lines show morphogen profiles computed for the case of a finite growth rate g for two values of g, solid lines show morphogen profiles in the limit case of slow growth as considered in Fig. 2B. Corresponding kymographs of computed tissue growth analogous to Fig. 2B are shown to the right. *C, D.* Final system size L^* normalized by pattern length-scale λ as function of a normalized growth threshold $\Theta\beta/\alpha w$ for the one-morphogen growth rule. Also shown are values of final system size for selected growth rates. *E.* Final system size L^* for fast growth, normalized by the system size $L^*_{\text{adiabatic}}$ for the adiabatic limit of slow growth $g \ll \beta$, as a function of the respective growth parameter (g, G, or γ) for different growth rules. In addition to the two-morphogen and one-morphogen growth rule introduced in the main text, we investigated two variants of the two-morphogen growth rule with growth rates g that vary either in time or space: *Absolute growth*, where the system grows with a growth rate $g(x) = G/L$ at all positions x where the concentrations $s(x)$ and $f(x)$ of both morphogens exceed the fixed threshold Θ; hence, the absolute change of system size per unit time, normalized by the relative size of the growth zone, is constant. and unit length is constant, as well as a *relative-overlap growth rule*, where the system grows at all positions x where the concentrations $s(x)$ and $f(x)$ exceed the threshold Θ with a spatially inhomogeneous growth rate $g(x) = \gamma[s(x) - \Theta][f(x) - \Theta]$ that depends on the relative overlap of the two morphogen profiles. We find that the final system size L^* is virtually independent of the rate of growth for the two-morphogen growth rule and its variants, but decreases for faster growth for the one-morphogen growth rule. Parameters: see Table S1, except growth thresholds for one-morphogen growth rule $\Theta = 0.25$, for two-morphogen growth rule $\Theta = 0.1379$.

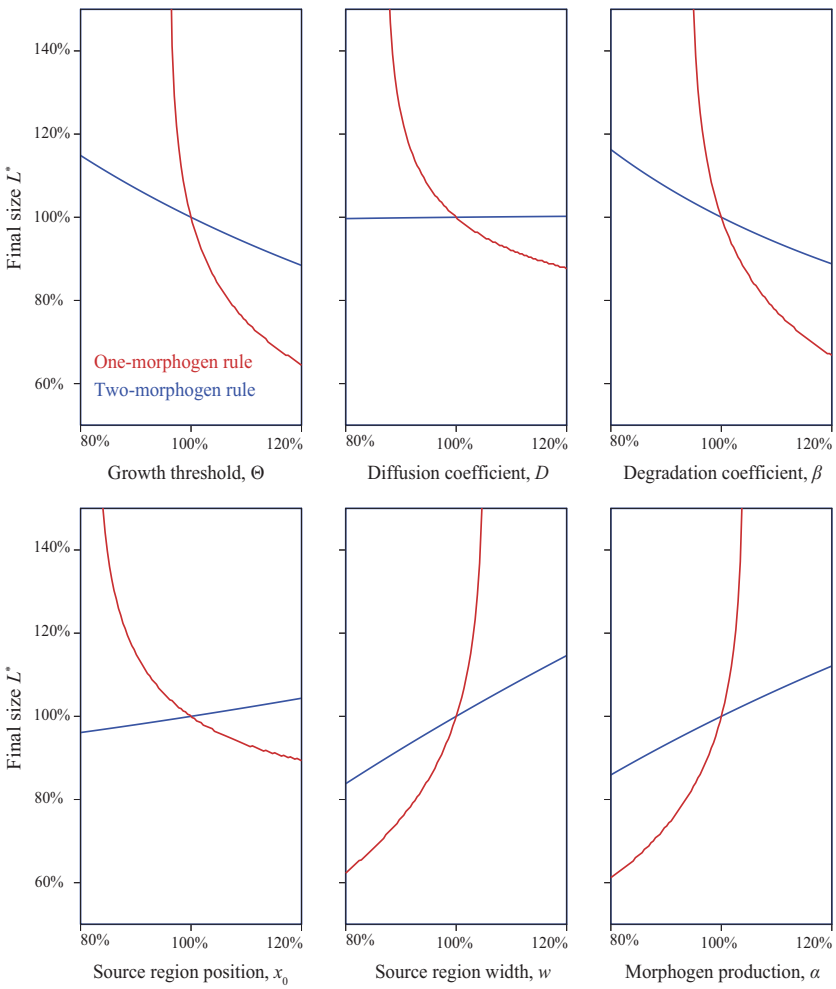

Figure S6. *Sensitivity of final system size to variations of model parameters.* Plots show the final system size L^* as function of all model parameters: growth threshold Θ, diffusion coefficient D, degradation coefficient β, source region position x_0 and its width w, production rate α. Red lines correspond to the one-morphogen growth rule and blue to the two-morphogen growth rule. Parameters in Table S1 correspond to 100%; for the growth threshold, we used as reference value $\Theta = 0.25$ for the one-morphogen growth rule, and $\Theta = 0.1379$ for two-morphogen growth rule (same as in Figure S5C-E).

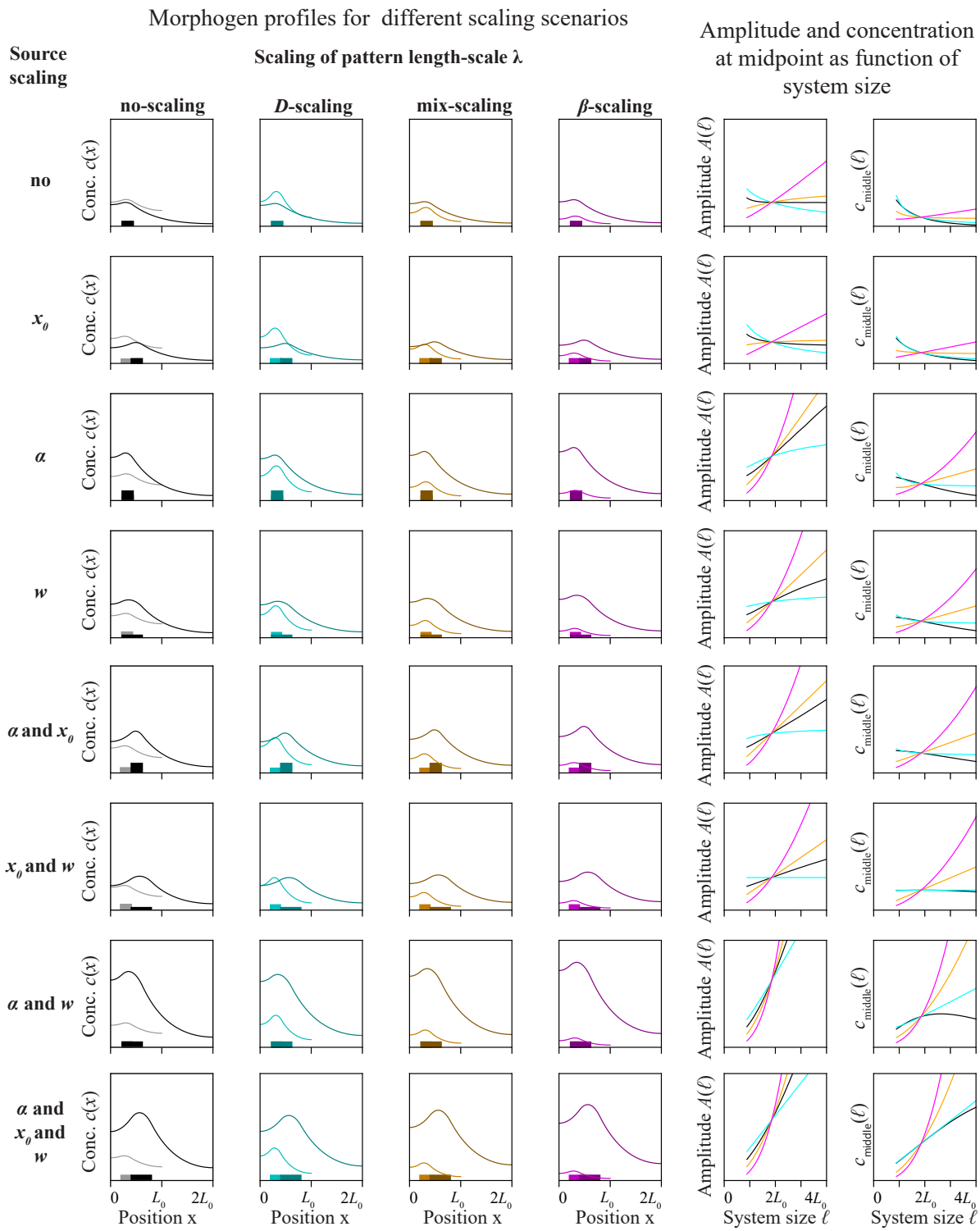

Figure S7. *Testing all scaling sub-scenarios for 5 model parameters.* The model parameters are: three parameters describing the source region: source width w, source position x_0, production rate α; and two parameters defining the pattern length-scale $\lambda = \sqrt{D/\beta}$, which can scale according to either D-scaling ($D \sim \ell^2$), mixed-scaling ($D \sim \ell$ and $\beta \sim 1/\ell$), or β-scaling ($\beta \sim 1/\ell^2$). The left side of the figure shows the overlaid morphogen profiles for two system sizes ℓ_0 and $2\ell_0$, (analogous to Fig. 2A) for each scaling sub-scenarios corresponding to the different combinations of source-parameter scaling (rows) and pattern length-scale-scaling (columns). The right side shows the amplitude and the concentration at the midpoint of morphogen profiles as function of system size ℓ for different scaling sub-scenarios, colored analogously to the left panel. To enable growth arrest in the case of the one-morphogen growth rule, the morphogen gradient amplitude must decay with ℓ; in the case of the two-morphogen growth rule, the morphogen concentration at the midpoint must decay with ℓ. Parameters: same as in Table S1.

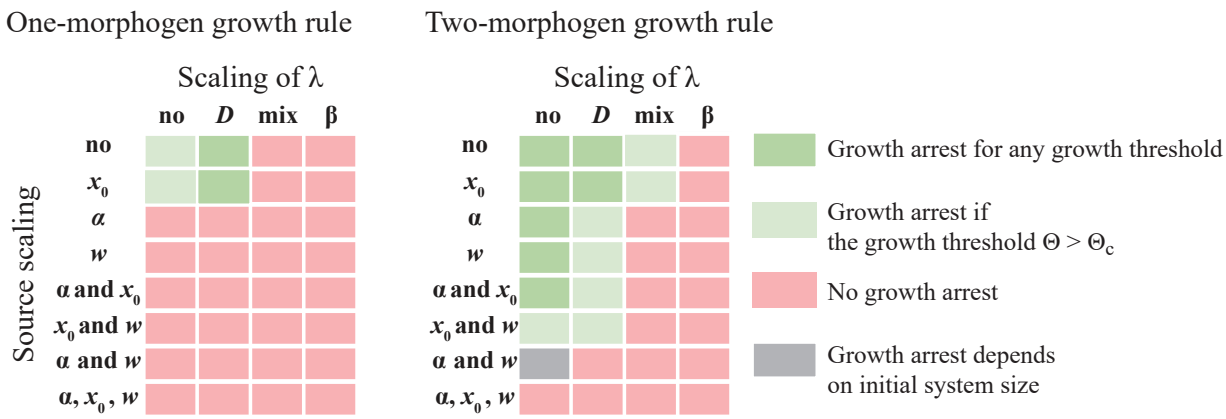

Figure S8. *Graphical summary of growth arrest for all scaling sub-scenarios for scaling of 5 model parameters for the scenario of dynamic scaling with blastema size.* Rows correspond to different sub-scenarios of source parameters (position x_0, width w, production rate α) that may scale with blastema size $L(t)$; columns correspond to different sub-scenarios of morphogen gradient parameters that may scale with $L(t)$, analogous to Fig. S7. For each sub-scenario of parameter scaling, it is indicated whether growth arrests for all choices of the growth threshold Θ (green), growth arrests if the growth threshold Θ exceeds a critical value Θ_c (light green), growth never arrests (red), or growth arrests only if the initial system size is smaller than a critical system size (gray).

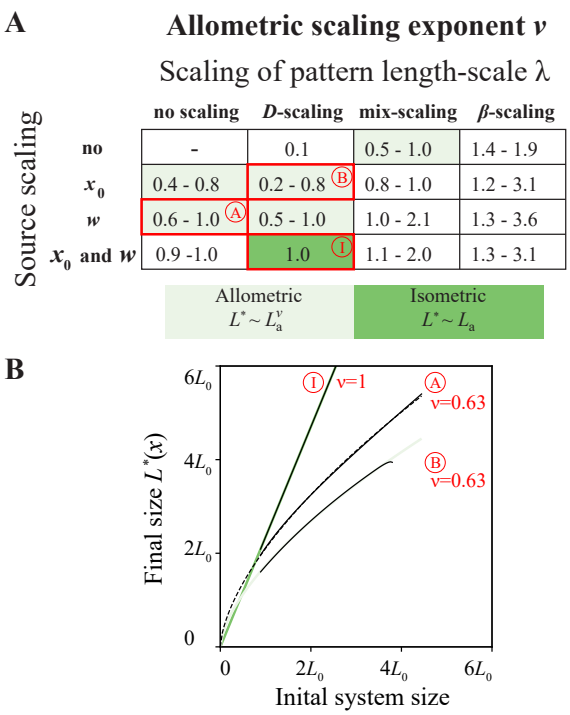

Figure S9. *Graphical summary of allometric scaling relations for static scaling with animal size.* *A.* Predicted scaling exponents ν of allometric scaling relations $L^* \sim L_a^\nu$ between final system size L^* and initial system size (assumed proportional to animal size L_a) for different sub-scenarios of static scaling with animal size for the two-morphogen growth rule. We systematically tested combinations of different sub-scenarios for the scaling of source size parameters with animal size (position x_0, width w; rows) and the scaling of the pattern length-scale λ with animal size L_a (columns), and report the range of exponents ν obtained by fitting a power law $L^* \sim L_a^\nu$ to solutions of Eq. S29 for different values for λ, w, x_0 (specified below). Only fits with a determination coefficient $R^2 > 0.95$ were included. *B.* Final system size L^* as a function of initial system size for three selected scaling sub-scenarios (highlighted in panel A): I: scaling of source position and width combined with D-scaling of pattern length-scale λ, resulting in proportional growth, A: scaling of source width without scaling of λ, and B: scaling of source position combined with D-scaling. R^2 was 1.0 in all three cases; the allometric scaling exponent $\nu = 0.63$ for A and B, which is close to the allometric scaling exponent observed for late-bud-stage blastemas (8) (see also Fig. S2). (Note that a more accurate comparison would refer to the ratio of allometric scaling exponents at the beginning and end of the first phase of blastema outgrowth, corresponding to the relative growth during this first growth phase. From the scaling exponents 0.61 and 0.43 for late-bud-stage blastemas and blastemas during subsequent digit cartilage formation several days later, respectively (8), we conclude that this ratio is likely smaller than 0.70=0.43/0.61.) Parameters: same as Table S1, with growth threshold $\Theta = 0.15$; in panel A, λ/L_a was varied in the range 0.01–0.9, $w/L_a = x_0/L_a$ was varied in the range 0–0.5; in panel B, $\lambda/L_a = 0.18$ and $w/L_a = x_0/L_a = 0.48$.

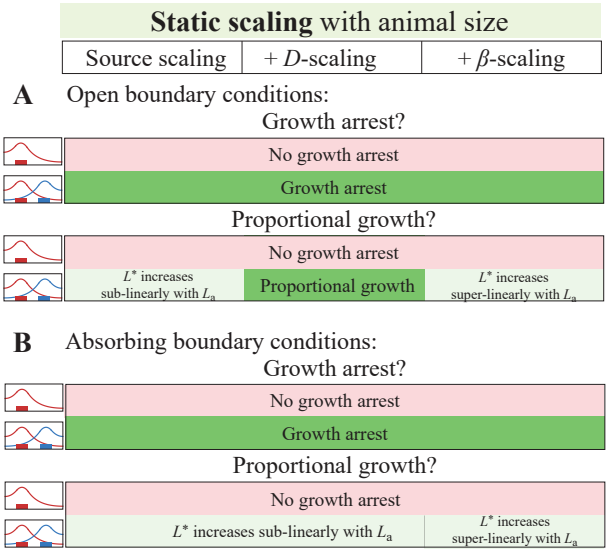

Figure S10. *Growth arrest and proportional scaling for static scaling scenario for different boundary conditions.* Analysis analogous to Fig. 2D, yet assuming either (A) open boundary conditions (by placing the finite system of size L inside a larger system), or (B) absorbing boundary conditions (by imposing the boundary conditions $s(x{=}0) = f(x{=}0) = s(x{=}L) = f(x{=}L) = 0$) instead of the reflecting boundary conditions used for Fig. 2D). Note that for the dynamic scaling scenario, results are identical to those of Fig. 2C when using either open or absorbing boundary conditions.

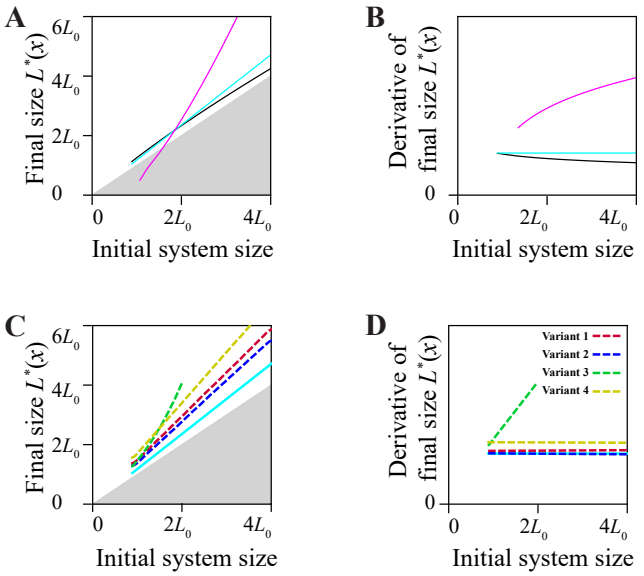

E

Parameter	Variant 1	Variant 2	Variant 3	Variant 4
w for SHH	dynamic	dynamic	dynamic	dynamic
x_0 for SHH	dynamic	dynamic	dynamic	dynamic
λ for SHH	dynamic	static	static	dynamic
w for FGF8	static	static	static	static
x_0 for FGF8	static	static	dynamic	dynamic
λ for FGF8	static	dynamic	dynamic	dynamic

	Growth arrest?
Two-morphogen	for D-scaling

	Proportional growth?		
Two-morphogen	for D-scaling	super-linearly	

Figure S11. *Proportional growth for mixed scaling scenarios.* For reference, panels A and B address scenarios of only static scaling of morphogen gradient parameters as shown in Fig. 2 in the main text, while panels C, D and E address variants of mixed scaling in which some parameters display dynamic scaling and others exhibit static scaling. *A.* Final system size as function of initial system size (assumed proportional to L_a) for three gradient scaling sub-scenarios as in Fig. 2: source scaling (black), $+D$-scaling (cyan), $+\beta$-scaling (magenta). *B.* Numerical derivative of the final system size with respect to the initial system size for the data shown in Panel A, to discriminate between sub-linear growth (decreasing), proportional growth (constant), and super-linear growth (increasing). *C.* Final system size as a function of initial system size for mixed scaling scenarios combining static and dynamic scaling (listed in panel E, assuming D-scaling; dashed), as well as the result for static scaling with D-scaling from panel A for comparison (cyan). *D.* Numerical derivative of final system size with respect to initial system size for the data shown in Panel C. *E.* Variants of mixed scaling scenarios, where some morphogen gradient parameters exhibit dynamic scaling, while other parameters exhibit static scaling. For each variant, our model predicts growth arrest and approximate proportional growth if the two-morphogen growth rule and D-scaling is assumed. Parameters: same as in Table S1, growth threshold $\Theta = 0.15$.

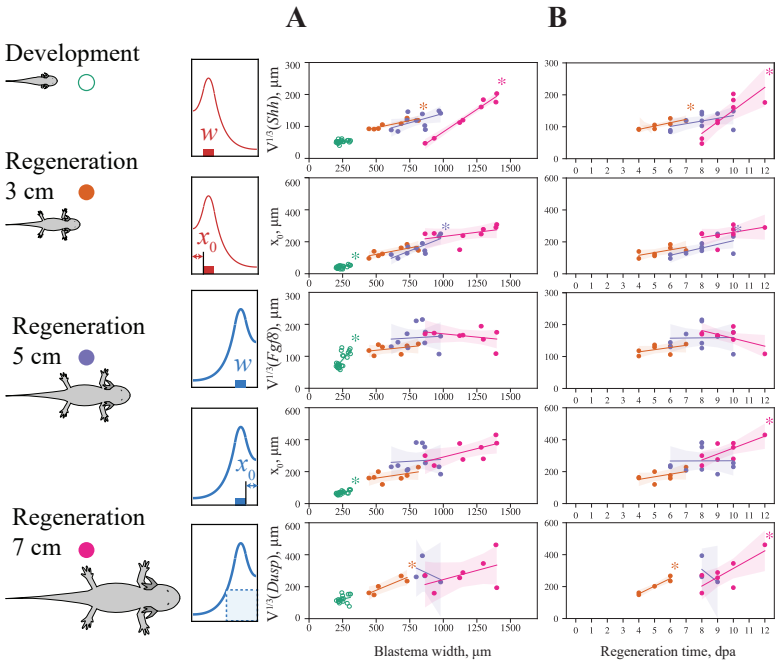

Figure S12. *Additional fit variant for Fig. 4D. A.* Same data as in Fig. 4D for experimentally measured characteristics of SHH and FGF8 source regions and signaling range, yet with separate linear regressions for each animal-size group. If a morphogen parameter displays dynamic scaling, regressions should have a significant positive slope, while for static scaling, the individual regressions should have a slope that is not statistically different from zero. *B.* Same data, yet with separate linear regressions for each animal-size group plotted against regeneration time. Again, if a morphogen parameter displays dynamic scaling, regressions should have a significant positive slope, while for static scaling, the individual regressions should have a slope that is not statistically different from zero. Stars indicate that the fitted slope from linear regression is statistically significantly different from zero ($p < 5\%$).

Parameter	Value
Diffusion coefficient D	$D_0 = 1$
Degradation rate β	$\beta_0 = 1$
Pattern length-scale λ	$\lambda_0 = \sqrt{D_0/\beta_0} = 1$
Production rate α	$\alpha_0 = 1$
Growth rate	$0.5\,\beta_0$
Source position x_0	$0.4\,\lambda_0$
Source width w	$0.4\,\lambda_0$
Initial size L_0	$1.8\,\lambda_0$
Proportionality coefficient λ/ℓ	0.3
Proportionality coefficient w/ℓ or x_0/ℓ	0.2

Table S1. *Non-dimensional parameter values used in numerical computations.* The morphogen parameters (diffusion coefficient D, degradation rate β, and production rate α) were set equal to 1; different values for these parameters correspond to trivial re-scaling of length units, time units, concentration units, and do not change any of our conclusions. The growth rate g was set to $g = 0.5\beta_0$ for most figures; other values of g are tested in Fig. S5. The source parameters (source position x_0, source width w) and proportionality coefficient assumed in morphogen gradient scaling were chosen to mimic the experimentally found values of these parameters (Fig. 4), normalized by the experimental estimate of FGF8 pattern length-scale.

	D-scaling $D \sim L^2$	Mixed-scaling $D \sim L; \beta \sim 1/L$	β-scaling $\beta \sim 1/L^2$
Amplitude	$\sim \frac{1}{L}$	Const	$\sim L$
Concentration at the midpoint	$\sim \frac{1}{L}$	Const	$\sim L$
	D-scaling $D \sim L_0^2$	Mixed-scaling $D \sim L_0; \beta \sim 1/L_0$	β-scaling $\beta \sim 1/L_0^2$
Final system size, one-morph. growth rule	$\sim$ arcoth$(C\ L_0)L_0$	$\sim L_0$	$\sim$ arcoth $\left(\frac{C}{L_0}\right) L_0$
Final system size, two-morph. growth rule	$\sim$ arcsinh$(\frac{C}{L_0})L_0$	$\sim L_0$	$\sim$ arcsinh$(CL_0)L_0$

Table S2. *Summary of analytical results.* In the limit case of a point source region, $w \to 0$, located at the left system boundary, $x_0 = 0$, the steady-state solution of the diffusion equation Eq. (1) is given by the analytical formula Eq. (S20). This table summaries how for Eq. (S20) the amplitude of the morphogen gradient profile and its concentration at the midpoint of the system depend on system size L for different sub-scenarios of dynamic scaling. Additionally, it is stated how the final system size L^* depends on the initial system size L_0 for different sub-scenarios of static scaling. Here, C denotes a constant factor that depends on the growth threshold Θ.

	Dynamic scaling with blastema size? *Null hypothesis:* static scaling		**Static scaling with animal size?** *Null hypothesis:* dynamic scaling	
Morphogen gradient parameter	Partial correl. analysis η^2	p	Partial correl. analysis η^2	p
w for SHH	0.58	<0.1%	0.19	n.s.
x_0 for SHH	0.54	<0.1%	<0.01	n.s.
w for FGF8	<0.01	n.s.	0.15	0.3%
x_0 for FGF8	0.14	0.5%	0.19	0.1%
$V^{1/3}$ for *Dusp6*	0.17	0.9%	<0.01	n.s.
L_a + noise	[-0.12,0.12]	n.s.	[0.25,0.48]	[<0.1%,5%]
L + noise	[0.24,0.47]	[<0.1%,6%]	[-0.13,0.14]	n.s.

Table S3. *Partial correlation analysis for morphogen gradient parameters against animal and blastema size.* Shown are the results of a partial correlation analysis for morphogen gradient parameters as reported in Fig. 4D, which allows testing for conditional statistical independence. To test for *dynamic scaling*, we aim to refute a null hypothesis of static scaling. We performed a partial correlation analysis against blastema size, after factoring out animal size. If the null hypothesis were true, no correlation should remain. Here, η^2 denotes the explained residual variance of a morphogen gradient parameter X due to the influence of blastema size $Y = L$ after factoring out the influence of animal size $Z = L_a$ according to Eq. S8, while p denotes the significance level of a positive linear correlation between blastema size and a morphogen parameter after factoring out animal size, computed using Eq. S11. A non-significant p-value is consistent with static scaling of this parameter, while a high η^2 and statistically significant p is indicative of *dynamic scaling*. To test for *static scaling*, we aim to refute a null hypothesis of dynamic scaling. We analogously performed a partial correlation analysis against animal size, after factoring out blastema size. Here, η^2 denotes the explained residual variance of a morphogen gradient parameter due to the influence of animal size $Y = L_a$ after factoring out the influence of blastema size $Z = L$, and p again the significance level of the corresponding correlation. A non-significant p-value is consistent with dynamic scaling of this parameter. For each morphogen parameter, $n = 48$ samples were analyzed, except $n = 33$ for *Dusp6*. Animal size corresponds to snout-to-tail animal length; snout-to-cloaca animal length gave very similar results. For comparison, we applied the same test also to synthetic data comprising $n = 48$ samples with the same animal and blastema sizes as measured in the experiments, and a hypothetical parameter X given by either animal size L_a or blastema size L multiplied by independent, normally distributed multiplicative noise factors with mean 1 and variance 0.25. Intervals for η^2 corresponds to the $[25\%, 75\%]$-inter quartile range.

Supplementary Methods

A. Numerical methods

As mentioned in the Methods section of the main text, in the presence of tissue growth with local growth rate $g(x,t)$, Eq. 1 changes to Eq. 4

$$\partial_t c(x,t) = D\,\partial_x^2 c(x,t) - v(x,t)\partial_x c(x,t) - [\beta + g(x,t)]c(x,t) + \alpha\,\chi_w(t)(x) \quad , \tag{S1}$$

where $\partial_x v = g$. Here, the growth-induced "dilution" term $-gc$ accounts for the fact that in a growing tissue the same amount of morphogen will be spread in an increasingly larger system, which decreases the local concentration c at a rate equal to the growth rate g (21; 46). To derive this term, note that Eq. S1 can be equivalently written as a continuity equation $\partial_t c = -\partial_x J - \beta c + \alpha\chi_w$, where $J = -D\partial_x c + vc$ is the combined current of morphogen molecules due to both diffusion with diffusion coefficient D and growth-induced advection with velocity v. By the product rule, $\partial_x(vc) = v(\partial_x c) + (\partial_x v)c = v\,\partial_x c + gc$ because $\partial_x v = g$, which naturally gives rise to the dilution term $-gc$ in Eq. S1.

This equation is numerically solved using a modified Euler scheme in a Lagrangian frame. While Eulerian coordinates describe fixed coordinate positions that are stationary with respect to a fixed laboratory frame, Lagrangian coordinates describe moving coordinates that track a particular point of a flowing material such as a growing tissue and thus move with its flow. Specifically, we consider a non-uniform spatial grid with grid points $x_i(t)$ in one space dimension, whose bin sizes $\Delta x_i(t_n) = x_{i+1}(t_n) - x_i(t_n)$ change in time according to

$$\Delta x_i(t_{n+1}) = [1 + g(x_i,t_n)\Delta t]\Delta x_i(t_n) \quad . \tag{S2}$$

The discretization of the Laplacian $\partial_x^2 c$ for this non-uniform grid reads

$$\partial_x^2 c(x_i,t_n) \approx \frac{2}{x_{i+1}(t_n) - x_{i-1}(t_n)} \left(\frac{c(x_{i+1},t_n) - c(x_i,t_n)}{x_{i+1}(t_n) - x_i(t_n)} - \frac{c(x_i,t_n) - c(x_{i-1},t_n)}{x_i(t_n) - x_{i-1}(t_n)} \right) \quad , \tag{S3}$$

where $c(x_i,t_n)$ is the concentration at position x_i and time t_n (more precisely, the average concentration in a spatial bin with center x_i), and x_i specifically denotes in this case the center of the spatial bin with the varying size. Note that the above Laplacian for the non-uniform grid reduces to the standard second-central-difference formula $c(x_{i+1},t_n) - 2c(x_i,t_n) + c(x_{i-1},t_n)/\Delta x^2$ if the grid spacing is uniform $x_{i+1}(t_n) - x_i(t_n) = x_i(t_n) - x_{i-1}(t_n) = \Delta x$. For the diffusion equation Eq. 4, the numerical Euler step reads

$$c_i(t_{n+1}) = c_i(t_n) - \Delta t\,(\beta + g)c_i(t_n) + \Delta t\,D\frac{2}{x_{i+1} - x_{i-1}} \left(\frac{c_{i+1}(t_n) - c_i(t_n)}{x_{i+1} - x_i} - \frac{c_i(t_n) - c_{i-1}(t_n)}{x_i - x_{i-1}} \right) + \Delta t\,\alpha\,\chi_w(x_i) \quad . \tag{S4}$$

Numerical stability requires that a Courant criterion $2D\,\Delta t \leq \Delta x^2$ is satisfied.

We confirmed in selected simulations that a conventional numerical scheme using Eulerian coordinates gives identical results. Specifically, for these tests, we employed fixed spatial bins with bin centers x_i and retained the advection term $v\partial_x c$ from Eq. (S1), which was discretized according to an upwind scheme, where we made use of $v_i \geq 0$. Compared to Eq. S4, the Euler step thus contains an additional advection term and reads

$$c_i(t_{n+1}) = c_i(t_n) + \text{degradation} + \text{diffusion} + \text{production} + v_i(t_n) \left(\frac{c_i(t_n) - c_{i-1}(t_n)}{x_i - x_{i-1}} \right) \quad . \tag{S5}$$

This numerical scheme with Eulerian coordinates imposes an additional criterion on the timestep Δt for the Euler scheme $|v|\,\Delta t \leq \Delta x$. If speeds v become large, this criterion can be much more restrictive than the Courant criterion for the diffusion term. As a consequence, computations using Eulerian coordinates require smaller time-steps to achieve the same accuracy as computations using Lagrangian coordinates.

B. Image analysis

First, all 3D images were re-binned for isotropic voxel size with dimensions $2 \times 2 \times 2$ μm, then rotated and cropped in 3D with Napari (49). Blastemas were segmented using APOC (48), trained with user-specified ground truth labels marking the tissue and the outside areas, respectively, and applied to the *Shh* channel. A constant background, corresponding to the mean intensity outside the segmented blastema, was subtracted from each channel. The blastema contained a significant number of blood cells, resulting in imaging artifacts across all channels. To address this issue, autofluorescence was acquired (499-nm illumination), and APOC segmentation was applied to this channel to identify a binary blood-vessel mask, which was subsequently excluded from all channels. Additionally, for some images, the intensity of the *Shh* channel decayed significantly along the z-axis. This artifact was corrected

by normalizing the *Shh* intensity along the axis using the intensity profile calculated at the most anterior edge of the tissue, outside the possible *Shh* region.

The *Shh*, *Fgf8*, and *Dusp6* channels were denoised using a 3D Gaussian blur with a standard deviation of $10\ \mu$m (5 pixels), followed by min-max normalization. The SHH and FGF8 source regions, as well as the FGF8 signaling range region indicated by *Dusp6* mRNA in 3D, were determined as regions enclosed by the respective 50%-iso-intensity surfaces. Small disconnected components were manually removed from the volumes enclosed by these iso-intensity surfaces. The linear size of these regions were determined as the cubic roots of the volumes enclosed by the respective surfaces. Choosing different iso-intensity surfaces, i.e., at 40% or 60% relative intensity, gave the same qualitative conclusions about scaling as Fig. 4.

Blastema size was measured in 3D images along a line passing through the centers-of-mass of the *Shh* and the *Fgf8* regions, as indicated in Fig. 4A, inset. We will refer to this line as SF in the following. At late stages of development and regeneration, the *Fgf8* region starts to attain a non-convex shape, and eventually splits into two separate domains. To determine the gap (x_0) between the tissue boundary and the boundary of the *Shh* and *Fgf8* regions in a robust manner, even for non-convex shapes of source regions, we first projected the three-dimensional binary masks along the dorsal-ventral axis onto a 2D-plane (using a logical OR-operation along the projection axis). Here, the dorsal-ventral axis was determined as the axis among all axes perpendicular to the line SF that was maximally aligned to the principal axis with smallest singular value obtained by a principal-component analysis (PCA) of the binary mask of the limb bud or blastema. The outlines of these projections are shown in Fig. 4A. We then measured the distance x_0 between the tissue boundary and the boundary of each source region in this 2D projection along the line SF. For the visualization in Fig. 4, 2D-projections of different samples corresponding to the same animal size and time-point were aligned by registering the midpoint and orientation of the line segment $\overline{SF}$ connecting the centers-of-mass S and F of the *Shh* and *Fgf8* regions. Limb buds stages were assigned as introduced in (50).

C. Experimental Methods

Animal breeding. Larval axolotls (*Ambystoma mexicanum*) were maintained at the axolotl facility at CRTD TU Dresden as described (51). Optimized axolotl (*Ambystoma mexicanum*) husbandry, breeding, metamorphosis, transgenesis and tamoxifen-mediated recombination were applied as in (51). All procedures were performed according to the Animal Ethics Committee of the State of Saxony, Germany. Animals of the d/d genetic backgrounds with body length in the range 1.2-9 cm were used for the HCR staining. For live measurements of blastema size, axolotls of the ZRS>TFP background (tgSceI(ZRS:TFPnls-T2A-ERT2-Cre-ERT2)^{Etnka} (16) with body length in the range 1.2-25 cm length were used.

Limb amputation and tissue collection Axolotls were anesthetized in 0.01% benzocaine solution for approximately 20 minutes. Sleeping animals were placed on a clean Petri dish to image and measure the size of the limb. Limbs were amputated using a scalpel such that the distal quarter of the zeugopod was removed and the protruding radius and ulna were trimmed with scissors to create a flat surface. To monitor the progress of regeneration, the animals were again anesthetized in 0.01% benzocaine and imaged using a SZX16 wide field microscope with bright field illumination or UV light for the ZRS>TFP line to visualize the expression of TFP protein. Prior to tissue collection, the animals were anesthetized and limbs were imaged to record the blastema stage. For staining, limbs were cut off at the shoulder level and fixed in MEMFA (0.1 M MOPS pH 7.4, 2 mM EGTA, 1 mM MgSO4·7H2O and 3.7% formaldehyde) for at least 3 days at 4°C. For qPCR, only blastema and a sliver of 0.5-1 mm of tissue behind the amputation plane were collected, immediately frozen in liquid nitrogen and kept at -70°C until use.

Whole-mount HCR *in situ* hybridization and tissue clearing. Target transcripts were identified in the axolotl transcriptome Amex.T_v47 (52) and confirmed by BLASTX alignment to the NCBI Refseq Protein Database. HCR probe pairs were designed by the `https://probegenerator.herokuapp.com/` probe generator, which uses Bowtie2 (53) to exclude probes that hit multiple genomic regions in the 60DD axolotl genome. Probe pairs (30-40 per target transcript) were ordered as oPools from Integrated DNA Technologies. Other consumables, including hybridization, wash and amplification buffers, as well as HCR hairpins were purchased from Molecular Instruments. RNA staining was done using the whole-mount HCR protocol from (47) with the following modifications. Tissues were collected and fixed in MEMFA (3.7% formaldehyde in MEM buffer) for >3 days at 4°C. Fixative was washed out by 3 × 15 minute washes in PBST (PBS +0.1% Tween), dehydrated with 25%, 50%, and 75% MeOH in PBST all on ice and finally stored at -20°C until use (up to 2 years). After re-hydration, the permeabilization step using Proteinase K was omitted and replaced by delipidation in boric acid buffer (200 mM boric acid, 4% SDS at pH8.5) for 2-4 h at room temperature, and permeabilization in 2% TritonX-100, 0.3M glycine, 20% DMSO in PBS either at 20°C or 37°C, for 12-14h. In the detection step, the initiator pools for all target genes of interest were combined, with the concentration of each initiator pool in the hybridization solution increased to 20 nM and the reaction extended to 20 h. In the signal amplification step, Alexa-546, Alexa-647 and Alexa-750 conjugated hairpins were used at 60 nM

each to detect Fgf8, Dusp6 and Shh mRNA, respectively. Both the detection and amplification steps were extended to 20-24 h. Following the final washes of the amplification step, nuclei were stained by incubation in 5xSSCT with DAPI (4,6-diamidino-2-phenylindole Sigma, #D9542) overnight at 4°C. For sample clearing, first, an equal amount of EasyIndex RI 1.52 (LifeCanvas Technologies) was added for 1 day at 4°C. Limbs were glued into a homemade vessel and covered with 100% EasyIndex for 3-10 days prior to imaging. All incubation steps were performed on a shaker or rocker. In all steps following the addition of the amplifiers, the samples were protected from light.

Whole-mount imaging. The whole-mount imaging was performed using an upright laser scanning confocal microscope Stellaris 8 (Leica) with a long range pulsed white light laser (flexible range 440-790 nm) and a pulsed 405-nm laser. For detection, LAS X software and a HC FLUOTAR L 16x/0,60 IMM CORR VISIR (11506533) Mag=16x, NA=0.6, WD=2.5mm, objective were used. The detection objective was set to match the RI of the clearing media (1.52) prior to imaging. HCR signal of Fgf8, Shh and Dusp6 was detected using the 557-nm, 752-nm and 653-nm excitation wavelength lasers. 499-nm illumination was used to detect autofluorescence. DAPI was illuminated with the 405-nm laser.

qPCR. RNA for RT–PCR was purified using RNeasy Mini Kit (Qiagen Cat. No. 74104). Reverse transcription was performed using SuperScript™ IV Reverse Transcriptase (Invitrogen^{TM}, Can. No.15387686) and Oligo dT17V as a primer. The quantitative PCR was performed using TB Green® Premix Ex Taq^{TM} (Tli RNase H Plus) kit (Takara, Cat. No. RR420L).
The following primers were used:

Target gene	Forward	Reverse
Fgf8	829 CCGCATTAAAGGAGCCGAGA	830 ATGAGGCTCCGTTGTTTGGT
Dusp6	340 CCAGGACTGTCTCAAAGATTCTGC	341 GCCTTCCGCAAGCATACATTG
Shh	806 GCTCTGTGAAAGCAGAGAACTCG	807 CGCTCCGTCTCTATCACGTAGAA
Ptch1	802 CGATCGAGAAAGTGAGGGCCATA	803 GAACTCCACTCCAATGCCAACAG
Rpl4	185 TGAAGAACTTGAGGGTCATGG	186 CTTGGCGTCTGCAGATTTTTT

Analysis was performed for two biological replicates. The parallel processing of samples should make individual normalized mRNA concentrations comparable for the two animal sizes.

D. Statistical Methods

Regression analysis. Unweighted linear regressions by least-square-fit for slope and intercept were performed for Figs. 1C, 4D. Statistical significance of non-zero slopes in Fig. 4D was confirmed by two-sided t-test at confidence level $\alpha = 0.05$. Fig. 4D, left and right columns, show linear regressions against blastema width L and animal size L_a (snout-to-tail), respectively.
For Fig. S3, linear regressions and power-law fits were performed, to test for isometric versus allometric scaling, respectively. The power-law exponents of allometric scaling obtained here perfectly match those reported by Furukawa et al. (8): Furukawa et al. reported exponents for the fitted allometric scaling relation between limb width and animal size of 0.90 ± 0.06 for fore limb and 0.91 ± 0.07 for hind limb, and an exponent 0.61 ± 0.03 for the fitted allometric scaling relationship between blastema width (late bud stage) and limb stump width (fit$\pm$SD from bootstrap), while our fits for our data gave an exponent of 0.92 ± 0.009 for the fitted allometric scaling relationship between fore limb width and animal length (snout-to-tail), and 0.63 ± 0.03 for the allometric scaling relationship between blastema width (mid/late stage) and limb width. Thus, the fitted scaling exponents almost perfectly match, although Furukawa et al. measured blastema width at the base of the blastema, while in this study (Fig. S2) blastema width was measured along a line that passes through the center of the TFP>ZRS reporter expression, parallel to the amputation plane, which is more distal towards the blastema tip compared to Furukawa, (correspondingly blastema widths are approximately 20% smaller compared to (8)). In addition to late-bud-stage blastemas, Furukawa et al. reported allometric scaling with exponent 0.43 ± 0.07 for blastema width as a function of limb width at the end of the first phase of blastema growth, shortly before the hypometric limb stage, when regenerated limbs had 3-4 cartilage condensations.)

Partial correlation analysis. To test for *dynamic scaling* versus *static scaling* of SHH and FGF8 morphogen gradient parameters, a partial correlation analysis was performed on the data presented in Fig. 4B as follows.
Let the observable X denote a morphogen gradient parameter. The statistical factors animal size $Z = L_a$ and blastema size $Y = L$ may both influence X. If the null hypothesis is that X exhibits *static scaling* with animal size, X should strongly correlate with Z, yet will be also correlated with Y because Y and Z are correlated. To factor out the effect of Z, we first performed separate linear regressions

$$X_i = \alpha_X + \beta_X Z_i + \varepsilon_{X,i} \text{ and } Y_i = \alpha_Y + \beta_Y Z_i + \varepsilon_{Y,i} \quad , \qquad \textbf{(S6)}$$

where $i = 1, \ldots, n$ enumerates the samples, and $\varepsilon_{X,i}$ and $\varepsilon_{Y,i}$ denote the respective residuals for X and Y. Next, we perform a linear regression between these residuals to reveal effects of Y on X not yet explained by Z

$$\varepsilon_{X,i} = \alpha + \beta \varepsilon_{Y,i} + \varepsilon_i \quad . \tag{S7}$$

The fraction η^2 of residual variance of X explained by Y after factoring out Z reads

$$\eta^2 = 1 - \frac{\sum_{i=1}^n \varepsilon_i^2}{\sum_{i=1}^n \varepsilon_{X,i}^2} \quad . \tag{S8}$$

The statistical significance of the effect of Y on X after factoring out Z can be tested as follows. Let r_{AB} denote the correlation coefficient between two variables A and B (Bravais-Pearson correlation)

$$r_{AB} = \frac{\sum_{i=1}^n (A_i - \overline{A})(B_i - \overline{B})}{\sqrt{\left(\sum_{i=1}^n \left(A_i - \overline{A}\right)^2\right)\left(\sum_{i=1}^n \left(B_i - \overline{B}\right)^2\right)}} \quad , \tag{S9}$$

where $\overline{A}$ and $\overline{B}$ denote the sample means of A and B, respectively. The *partial correlation coefficient* $r_{XY,Z}$ between X and Y after factoring out Z is then given by (54)

$$r_{XY,Z} = \frac{r_{XY} - r_{XZ} r_{YZ}}{\sqrt{\left(1 - r_{XZ}^2\right)\left(1 - r_{YZ}^2\right)}} \quad . \tag{S10}$$

If the null hypothesis that Y has no effect on X after factoring out Z is true (and errors are independent and distributed normally with equal variance), the derived test-variable $t_{XY,Z}$ obeys a t-distribution with $n-3$ degrees of freedom

$$t_{XY,Z} = \sqrt{n-3} \frac{r_{XY,Z}}{\sqrt{1 - r_{XY,Z}^2}} \quad . \tag{S11}$$

Now, p-values of a one-sided t-test can be readily computed. To test for the null hypothesis that a morphogen gradient parameter X exhibits *dynamic scaling*, the above analysis can be repeated with the roles of Y and Z swapped. Results are reported in Table S3. The data reported in Fig. 4B is thus compatible with dynamic scaling of source region size w and source position x_0 for SHH, and static scaling of source region size w for FGF8. For computations, the Python package `causal-learn` was used.

Supplementary Information for Mathematical Modeling

E. Steady-state solutions of diffusion equation

Finite system size and extended source region. We recall Eq. 1 from the main text

$$\partial_t c(x,t) = D \partial_x^2 c(x,t) - \beta c(x,t) + \alpha \chi(x) \quad . \tag{S12}$$

We assume reflecting boundary conditions, i.e., no flux of morphogens at the system's boundaries $x = 0$ and $x = L$

$$\partial_x c(x)|_{x=0} = \partial_x c(x)|_{x=L} = 0 \quad . \tag{S13}$$

At steady state, Eq. 1 reduces to

$$0 = \lambda^2 \partial_x^2 c(x,t) - c(x,t) + \frac{\alpha}{\beta} \chi(x) \quad , \tag{S14}$$

where $\lambda = (D/\beta)^{1/2}$ denotes the pattern length-scale as introduced in the main text. The Green's function for the differential operator $\lambda^2 \partial^2 - 1$ with reflective boundary conditions Eq. S13 reads

$$G(x,s) = \frac{1}{\lambda \sinh \frac{L}{\lambda}} \left[\cosh\left(\frac{L-s}{\lambda}\right) \cosh\left(\frac{x}{\lambda}\right) \Theta(s-x) + \cosh\left(\frac{s}{\lambda}\right) \cosh\left(\frac{L-x}{\lambda}\right) \Theta(x-s) \right] \quad , \tag{S15}$$

where $\Theta(x)$ denotes the Heaviside step function. Thus, the steady state solution c^* of Eq. (1) can be written for an arbitrary source region described by a shape function $\chi(x)$ as

$$c^*(x) = \frac{\alpha}{\beta} \int_0^L G(x,s)\, \chi(s)\, ds \quad . \tag{S16}$$

For the source function introduced in the main text

$$\chi_w(x) = \Theta(w + x_0 - x)\Theta(x - x_0) \quad , \tag{S17}$$

which takes the constant value 1 inside the interval $[x_0, x_0 + w]$ and zero outside, the steady state solution c^* reads

$$c^*(x) = \frac{\alpha}{\beta \sinh \frac{L}{\lambda}} \begin{cases} 2\sinh\frac{w}{2\lambda}\cosh\frac{2L-(w+2x_0)}{2\lambda}\cosh\frac{x}{\lambda}, & x \in (0, x_0) \\ \sinh\frac{L}{\lambda} - \left(\sinh\frac{L-w-x_0}{\lambda}\cosh\frac{x}{\lambda} + \sinh\frac{x_0}{\lambda}\cosh\frac{L-x}{\lambda}\right), & x \in [x_0, x_0+w] \\ 2\sinh\frac{w}{2\lambda}\cosh\frac{w+2x_0}{2\lambda}\cosh\frac{L-x}{\lambda}. & x \in (x_0+w, L) \end{cases} \tag{S18}$$

Point source region. To facilitate analytical analysis of growth arrest and morphogen gradient scaling as function of key model parameters (diffusion coefficient D, degradation rate β, and total production rate $j = \alpha w$), we state the steady-state solution of Eq. (S18) for a point morphogen source region located at $x = x_0$, corresponding to the limit $w \to 0$ with $j = \alpha w =$ const.

$$c^*(x) = \frac{\alpha w}{\sqrt{D\beta}\sinh\frac{L}{\lambda}} \begin{cases} \cosh\frac{L-x_0}{\lambda}\cosh\frac{x}{\lambda}, & x \in (0, x_0] \\ \cosh\frac{x_0}{\lambda}\cosh\frac{L-x}{\lambda}. & x \in (x_0, L) \end{cases} \tag{S19}$$

Point source region at system boundary. For sake of completeness, we additionally state the steady-state solution of Eq. 1 for a point source located the the system boundary $x_0 = 0$

$$c^*(x) = \frac{\alpha w}{\sqrt{D\beta}\sinh\frac{L}{\lambda}}\cosh\frac{L-x}{\lambda} \quad . \tag{S20}$$

As a technical point, the no-flux boundary condition S13 needs to be modified for a point source located at the system boundary such that the diffusive flux equals morphogen production, $-D\partial_x c_{|x=0} = j$.

Point source region in an unbounded system. In the limit of an unbounded system with $L \to +\infty$, the steady-state solution Eq. S20 further simplifies to

$$c^*(x) = \frac{\alpha w}{\sqrt{D\beta}}\exp\left(-\frac{x}{\lambda}\right) \quad , \tag{S21}$$

corresponding to Eq. (3) in the main text.

Point source region with absorbing boundary. Finally, one could assume absorbing boundary conditions, i.e., the system's boundaries $x = 0$ and $x = L$ act as perfect sinks, and morphogen concentrations must vanish there

$$c(0) = c(L) = 0 \quad . \tag{S22}$$

For this case, the steady-state solution for Eq. 1 for a point source located at x_0 reads

$$c^*(x) = \begin{cases} \frac{\alpha w \lambda}{D}\frac{\sinh\left(\frac{L-x_0}{\lambda}\right)\sinh\left(\frac{x}{\lambda}\right)}{\sinh\left(\frac{L}{\lambda}\right)}, & x \in (0, x_0] \\ \frac{\alpha w \lambda}{D}\frac{\sinh\left(\frac{x_0}{\lambda}\right)\sinh\left(\frac{L-x}{\lambda}\right)}{\sinh\left(\frac{L}{\lambda}\right)}, & x \in (x_0, L) \end{cases} \quad . \tag{S23}$$

F. Oppositely-oriented morphogen gradients at left and right system boundaries

As mentioned in main text, the degradation-diffusion model for morphogen dynamics Eq. (1) TODO can be generalized in a straight-forward manner to the case of two opposing morphogen gradients with respective concentration fields $s(x,t)$ and $f(x,t)$, which can be explicitly written as

$$\partial_t s(x,t) = D\,\partial_x^2 s(x,t) - \beta\, s(x,t) + \alpha\,\chi_s(x) \quad , \tag{S24}$$

$$\partial_t f(x,t) = D\,\partial_x^2 f(x,t) - \beta\, f(x,t) + \alpha\,\chi_f(x) \quad , \tag{S25}$$

where, for simplicity, the source regions are also mirror-symmetric, $\chi_s(x) = \chi_f(L-x)$.

G. Growth rules define the final system size as function of model parameters

One-morphogen growth rule. In the case of the one-morphogen growth rule, growth stops when the growth threshold Θ equals the morphogen gradient amplitude A. The final system size L^* is thus determined by the condition

$$L^*_{\text{one}} : A := \max_{[0,L^*]} c(x) \stackrel{!}{=} \Theta \quad . \tag{S26}$$

In the limit case of a point morphogen source Eq. S20, the final system size can be written as

$$L^*_{\text{one}} = \lambda \operatorname{arcoth}\left(\frac{\Theta\sqrt{D\beta}}{\alpha w}\right) \quad . \tag{S27}$$

The function $\operatorname{arcoth}\left(\frac{\Theta\sqrt{D\beta}}{\alpha w}\right)$ is defined only for $\frac{\Theta\sqrt{D\beta}}{\alpha w} > 0$, which gives the critical growth threshold Θ_{cr} for growth arrest for the one-morphogen growth rule as

$$\Theta_{\text{cr}} = \frac{\alpha w}{\sqrt{D\beta}} \quad . \tag{S28}$$

Two-morphogen growth rule. For the two-morphogen growth rule, growth stops when the growth threshold Θ equals the morphogen concentration at the intersection of the morphogen. For simplicity, we consider the symmetrical case, where both morphogens have identical parameters, but their source regions are located at opposite boundaries of the system. In this case, morphogen gradients intersect at the midpoint of the system; therefore, the final system size L^* is determined by

$$L^*_{\text{two}} : c\left(\frac{L^*}{2}\right) \stackrel{!}{=} \Theta \quad . \tag{S29}$$

In the limit case of point morphogen source, Eq. S20, the final system size can be written as

$$L^*_{\text{two}} = 2\lambda \operatorname{arcsinh}\left(\frac{\alpha w}{2\Theta\sqrt{D\beta}}\right) \quad . \tag{S30}$$

H. Mutual feedback between morphogens

In the main text, we introduced feedback between the two morphogens, where a morphogen can only be produced inside a competent zone at the boundary with width $w_{\text{competent}}$ if the other morphogen exceeds a fixed feedback threshold, Θ_{fb}. To obtain the phase diagram Fig. 5B, we define a separatrix that separates a regime dominated by the growth threshold Θ and a regime dominated by the feedback threshold Θ_{fb}. Specifically, the separatrix is defined by the condition that both thresholds can be reached simultaneously. Accordingly, the final source position x_0^* is both strictly positive and strictly smaller than $w_{\text{competent}}$.
In our minimal model, growth arrests only if the growth threshold Θ has been reached. For the two-morphogen growth rule, this occurs at the midpoint of system, see also Eq. S29. In this case, the source width equals $w_{\text{competent}} - x_0^*$. Hence, assuming that the growth threshold is reached outside the source region and using Eqs. S18 and S29, the growth threshold can be explicitly written as

$$\Theta = \frac{2\alpha}{\beta \sinh\left(\frac{L^*}{\lambda}\right)} \sinh\left(\frac{w_{\text{comp.}} - x_0^*}{2\lambda}\right) \cosh\left(\frac{2w_{\text{comp.}} + x_0^*}{2\lambda}\right) \cosh\left(\frac{L^*}{2\lambda}\right) \quad . \tag{S31}$$

For the case of symmetrical morphogens at two opposing sides of the system, we can also state the feedback threshold at the moment of growth arrest as the concentration at the position $x = L^* - x_0^*$, which can be written as

$$\Theta_{\text{fb}} = \frac{2\alpha}{\beta \sinh\left(\frac{L^*}{\lambda}\right)} \sinh\left(\frac{w_{\text{comp.}} - x_0^*}{2\lambda}\right) \cosh\left(\frac{2w_{\text{comp.}} + x_0^*}{2\lambda}\right) \cosh\left(\frac{x_0^*}{\lambda}\right) \quad . \tag{S32}$$

Assuming the critical situation, where $x_0^* = 0$ and varying the final system size L^* according to Eq. S31 and Eq. S32, we obtain the separatrix between the two regimes as shown in Fig. 5B.

Supplementary references

1. Simon A, Tanaka E (2013) Limb regeneration. *Wiley Interdisciplinary Reviews: Developmental Biology* 2(2):291–300.
2. Muneoka K, Bryant SV (1982) Evidence that patterning mechanisms in developing and regenerating limbs are the same. *Nature* 298(5872):369–371.
3. Payzin-Dogru D, Whited JL (2018) An integrative framework for salamander and mouse limb regeneration. *The International Journal of Developmental Biology* 62(6-7-8):393–402.

4. Young JJ, Tabin CJ (2017) Saunders's framework for understanding limb development as a platform for investigating limb evolution. *Developmental Biology* 429(2):401–408.
5. Vieira WA, Wells KM, McCusker CD (2020) Advancements to the axolotl model for regeneration and aging. *Gerontology* 66(3):212–222.
6. Leigh ND, Currie JD (2022) Rebuilding limbs, one cell at a time. *Developmental Dynamics* 251(9):1389.
7. Wells KM, Kelley K, Baumel M, Vieira WA, McCusker CD (2021) Neural control of growth and size in the axolotl limb regenerate. *eLife* 10:e68584.
8. Furukawa S, Yamamoto S, Ohashi A, Morishita Y, Satoh A (2024) Allometry in limb regeneration and scale-invariant patterning as the basis of normal morphogenesis from different sizes of blastemas. *Development* pp. dev–202697.
9. Torok MA, Gardiner DM, Izpisúa-Belmonte JC, Bryant SV (1999) Sonic hedgehog (SHH) expression in developing and regenerating axolotl limbs. *Journal of Experimental Zoology* 284(2):197–206.
10. Tickle C, Towers M (2017) Sonic hedgehog signaling in limb development. *Frontiers in Cell and Developmental Biology* 5:14.
11. Han MJ, An JY, Kim WS (2001) Expression patterns of FGF-8 during development and limb regeneration of the axolotl. *Developmental Dynamics* 220(1):40–48.
12. Purushothaman S, Elewa A, Seifert AW (2019) FGF-signaling is compartmentalized within the mesenchyme and controls proliferation during salamander limb development. *eLife* 8:e48507.
13. Laufer E, Nelson CE, Johnson RL, Morgan BA, Tabin C (1994) Sonic hedgehog and FGF-4 act through a signaling cascade and feedback loop to integrate growth and patterning of the developing limb bud. *Cell* 79(6):993–1003.
14. Niswander L, Jeffrey S, Martin GR, Tickle C (1994) A positive feedback loop coordinates growth and patterning in the vertebrate limb. *Nature* 371(6498):609–612.
15. Bénazet JD, et al. (2009) A self-regulatory system of interlinked signaling feedback loops controls mouse limb patterning. *Science* 323(5917):1050–1053.
16. Otsuki L, Plattner S, Taniguchi-Sugiura Y, Falcon F, Tanaka E (2025) Molecular basis of positional memory in limb regeneration. *Nature*.
17. Nacu E, Gromberg E, Oliveira CR, Drechsel D, Tanaka EM (2016) FGF8 and SHH substitute for anterior–posterior tissue interactions to induce limb regeneration. *Nature* 533(7603):407–410.
18. Glotzer GL, Tardivo P, Tanaka EM (2022) Canonical Wnt signaling and the regulation of divergent mesenchymal FGF8 expression in axolotl limb development and regeneration. *eLife* 11:e79762.
19. Wolpert L (1969) Positional information and the spatial pattern of cellular differentiation. *Journal of Theoretical Biology* 25(1):1–47.
20. Ben-Zvi D, Pyrowolakis G, Barkai N, Shilo BZ (2011) Expansion-repression mechanism for scaling the DPP activation gradient in *Drosophila* wing imaginal discs. *Current Biology* 21(16):1391–1396.
21. Wartlick O, et al. (2011) Dynamics of DPP signaling and proliferation control. *Science* 331(6021):1154–1159.
22. Stückemann T, et al. (2017) Antagonistic self-organizing patterning systems control maintenance and regeneration of the anteroposterior axis in planarians. *Developmental Cell* 40(3):248–263.
23. Mateus R, et al. (2020) BMP signaling gradient scaling in the zebrafish pectoral fin. *Cell reports* 30(12):4292–4302.
24. Romanova-Michaelides M, et al. (2022) Morphogen gradient scaling by recycling of intracellular DPP. *Nature* 602(7896):287–293.
25. Kicheva A, Briscoe J (2023) Control of tissue development by morphogens. *Annual Review of Cell and Developmental Biology* 39(1):91–121.
26. Nikolić M, et al. (2024) Scale invariance in early embryonic development. *Proc. Natl. Acad. Sci. U.S.A.* 121(46):e2403265121.
27. Rich A, et al. (2025) Decaying and expanding ERK gradients process memory of skeletal size during zebrafish fin regeneration. *bioRxiv* pp. 2025–01.
28. Molina GA, Watkins SC, Tsang M (2007) Generation of FGF reporter transgenic zebrafish and their utility in chemical screens. *BMC developmental biology* 7:1–14.
29. Li C, Scott DA, Hatch E, Tian X, Mansour SL (2007) Dusp6 (Mkp3) is a negative feedback regulator of FGF-stimulated ERK signaling during mouse development. *Development* 134(1):167–176.
30. Ekerot M, et al. (2008) Negative-feedback regulation of FGF signalling by DUSP6/MKP-3 is driven by ERK1/2 and mediated by Ets factor binding to a conserved site within the DUSP6/MKP-3 gene promoter. *Biochemical Journal* 412(2):287–298.
31. Carlson BM (1975) The effects of rotation and positional change of stump tissues upon morphogenesis of the regenerating axolotl limb. *Developmental Biology* 47(2):269–291.
32. Endo T, Bryant SV, Gardiner DM (2004) A stepwise model system for limb regeneration. *Developmental Biology* 270(1):135–145.
33. Bryant SV (1976) Regenerative failure of double half limbs in *Notophthalmus viridescens*. *Nature* 263(5579):676–679.
34. Ben-Zvi D, Barkai N (2010) Scaling of morphogen gradients by an expansion-repression integral feedback control. *Proc. Natl. Acad. Sci. U.S.A.* 107(15):6924–6929.
35. Werner S, et al. (2015) Scaling and regeneration of self-organized patterns. *Physical Review Letters* 114(13):138101.
36. Umulis DM, Othmer HG (2013) Mechanisms of scaling in pattern formation. *Development* 140(24):4830–4843.
37. Shilo BZ, Barkai N (2017) Buffering global variability of morphogen gradients. *Developmental Cell* 40(5):429–438.
38. Wartlick O, Mumcu P, Jülicher F, Gonzalez-Gaitan M (2011) Understanding morphogenetic growth control—lessons from flies. *Nature Reviews Molecular Cell Biology* 12(9):594–604.
39. Schlissel G, Meziane M, Narducci D, Hansen AS, Li P (2024) Diffusion barriers imposed by tissue topology shape hedgehog morphogen gradients. *Proc. Natl. Acad. Sci. U.S.A.* 121(36):e2400677121.
40. Collins ZM, Ishimatsu K, Tsai TY, Megason SG (2023) A Scube2-SHH feedback loop links morphogen release to morphogen signaling to enable scale invariant patterning of the ventral neural tube. *bioRxiv* https://doi.org/10.1101/469239.
41. Zuniga A, Zeller R (2020) Dynamic and self-regulatory interactions among gene regulatory networks control vertebrate limb bud morphogenesis. *Current Topics in Developmental Biology* 139:61–88.
42. Scherz PJ, Harfe BD, McMahon AP, Tabin CJ (2004) The limb bud SHH-FGF feedback loop is terminated by expansion of former ZPA cells. *Science* 305(5682):396–399.

43. Verheyden JM, Sun X (2008) An FGF/Gremlin inhibitory feedback loop triggers termination of limb bud outgrowth. *Nature* 454(7204):638–641.
44. Nissim S, Hasso SM, Fallon JF, Tabin CJ (2006) Regulation of Gremlin expression in the posterior limb bud. *Developmental Biology* 299(1):12–21.
45. Saiz-Lopez P, et al. (2015) An intrinsic timer specifies distal structures of the vertebrate limb. *Nature communications* 6(1):8108.
46. Aguilar-Hidalgo D, et al. (2018) Critical point in self-organized tissue growth. *Physical Review Letters* 120(19):198102.
47. Choi HM, et al. (2018) Third-generation *in situ* hybridization chain reaction: multiplexed, quantitative, sensitive, versatile, robust. *Development* 145(12):dev165753.
48. Haase R, Lee D, Pop DD, Žigutytė L (2023) napari-accelerated-pixel-and-object-classification: 0.14.1. *https://doi.org/10.5281/zenodo.10071078*.
49. Chiu CL, Clack N, et al. (2022) Napari: a Python multi-dimensional image viewer platform for the research community. *Microscopy and Microanalysis* 28(S1):1576–1577.
50. Nye HL, Cameron JA, Chernoff EA, Stocum DL (2003) Extending the table of stages of normal development of the axolotl: limb development. *Developmental dynamics: an official publication of the American Association of Anatomists* 226(3):555–560.
51. Khattak S, et al. (2014) Optimized axolotl (*Ambystoma mexicanum*) husbandry, breeding, metamorphosis, transgenesis and tamoxifen-mediated recombination. *Nature protocols* 9(3):529–540.
52. Schloissnig S, et al. (2021) The giant axolotl genome uncovers the evolution, scaling, and transcriptional control of complex gene loci. *Proc. Natl. Acad. Sci. U.S.A.* 118(15):e2017176118.
53. Langmead B, Salzberg SL (2012) Fast gapped-read alignment with bowtie 2. *Nature methods* 9(4):357–359.
54. Rudolf M, Kuhlisch W (2008) *Biostatistik: Eine Einführung für Biowissenschaftler*. (Cambridge University Press).